KaRIn, the Ka-Band Radar Interferometer of the SWOT Mission: Design and In-Flight Performance

Eva Peral, Daniel Esteban-Fernández, Ernesto Rodríguez, Dalia McWatters, Jan-Willem De Bleser, Razi Ahmed, Albert C. Chen, Eric Slimko, Ruwan Somawardhana, Kevin Knarr, Michael Johnson, Sermsak Jaruwatanadilok, Samuel Chan, Xiaoqing Wu, Duane Clark, Kenneth Peters, Curtis W. Chen, Peter Mao, Behrouz Khayatian, Jacqueline Chen, Richard E. Hodges, *Life Senior Member, IEEE*, Dhemetrios Boussalis, Bryan Stiles, *Member, IEEE*, and Karthik Srinivasan

***Abstract*— The Surface Water and Ocean Topography (SWOT) mission was recommended by the 2007 National Research Council Decadal Survey to expand on previous altimetry missions such as TOPEX/Poseidon. Utilizing wide-swath altimetry technology, SWOT aims to achieve complete coverage of the world's oceans and freshwater bodies through high-resolution elevation measurements. SWOT received approval for implementation in 2016, it was ultimately launched in December 2022, and it is currently delivering preliminary data to the public. The primary instrument in SWOT is the Ka-band Radar Interferometer (KaRIn), which utilizes Jet Propulsion Laboratory (JPL)-developed radar interferometry technology to measure ocean and surface water levels with unprecedented accuracy. This article focuses on the challenges in designing, testing, and finally commissioning in flight a complex instrument such as KaRIn. We also present preliminary flight performance and compare it with ground measurements and simulations. Our analysis indicates that KaRIn meets or exceeds all its requirements, but it has also revealed several interesting and unexpected observations, offering just a glimpse of future scientific discoveries that KaRIn will enable.**

***Index Terms*— Ocean circulation, radar interferometry, surface water.**

NOMENCLATURE

ADC	Analog-to-digital converter.
ARW	Angular random walk.
BTM	Bit-true model.
DQA	Data quality analyzer.
DTS	Digital target simulator.
EIK	Extended interaction klystron.
FODL	Fiber optic delay line.
FSW	Flight software.
HPA	High-power amplifier.
HR	High resolution.
IMU	Inertial motion unit.
KDES	KaRIn digital electronics subsystem.
LDR	Linear depolarization ratio.
LO	Local oscillator.
LR	Low resolution.
OBP	Onboard processing.
POD	Precision orbit determination.
PSD	Power spectral density.
RFU	RF unit.
RMS	Root mean square.
S/C	Spacecraft.
SAR	Synthetic aperture radar.
SDR	Surface differential reflectivity.
SLC	Single-look complex.
SNR	Signal-to-noise ratio.
SSB	Sea-state bias.
SSH	Sea surface height.
SSHA	Sea surface height anomaly.
SWH	Significant wave height.

Manuscript received 11 January 2024; revised 28 March 2024; accepted 2 May 2024. Date of publication 24 May 2024; date of current version 13 June 2024. This work was supported by the Jet Propulsion Laboratory, California Institute of Technology, through the National Aeronautics and Space Administration under Contract 80NM0018D0004. Government sponsorship acknowledged. *(Corresponding author: Eva Peral.)*

The authors are with the Jet Propulsion Laboratory (JPL), California Institute of Technology, Pasadena, CA 91011 USA (e-mail: Eva.Peral@jpl.nasa.gov).

Digital Object Identifier 10.1109/TGRS.2024.3405343

I. INTRODUCTION

THE elevation of surface water and its slope relative to a reference surface (e.g., the Earth's geoid) plays an important part in determining the circulation of the ocean [1] and the storage and discharge of fresh water over land surfaces [2]. Until 2023, the best source for obtaining these data on a global basis was the coordinated use of multiple nadir radar altimeters [3]. Over the ocean, multiple nadir altimeters (NAs) can be combined to provide a spatial resolution varying between 100 km at mid-altitudes and 800 km in the tropics [1], [4]. This is too coarse to capture small mesoscale and submesoscale currents, which are important in understanding the ocean's vertical dynamics. Similarly, the sparse sampling of water bodies over land by a constellation of altimeters leaves many major lakes and rivers unobserved [5].

To overcome this coverage gap, the concept of *wide-swath altimetry* (see [6] for a review), which obtains high-precision elevation measurements over a swath and thus filling the coverage holes left by altimeters, was introduced. The basic

idea is to use radar interferometry [7], [8] at near-nadir incidence angles, enabling centimetric-level accuracy of height measurements in contrast to the meter-level accuracy that is characteristic of moderate incidence angles from space [9]. This concept was endorsed by the 2007 National Research Council Decadal Survey [10]. Following this recommendation, the United States National Aeronautics and Space Administration (NASA) and the French Centre National d'Etudes Spatiales (CNES) (with additional contributions from Canada and U.K.) partnered in building the Surface Water and Ocean Topography (SWOT) mission [11], which launched in December 2022 and is now delivering preliminary data to the science community.

The heart of the SWOT mission is Ka-band Radar Interferometer (KaRIn), whose design, engineering choices, error budget, and post-flight performance we will review here. In Section II, we review the SWOT mission history, the driving ocean and hydrology measurement requirements, and the allocated pre-launch error budget, all of which drove the instrument parameters. In Section III, we present the main components of the KaRIn instrument, which contains many innovations that were necessary to enable the instrument to meet its stringent requirements: OBP of interferometric data, ultrastable interferometric masts and IMU, deployable reflectarray antennas at Ka-band, a stable and high-power Ka-band RF chain, and detailed system-wide modeling. In Section IV, we review the pre-launch performance verification, and in Sections V and VI, we review the performance results obtained during the commissioning phase.

II. SWOT Mission Overview

SWOT is an international partnership between NASA and CNES, with contributions from Canadian Space Agency (CSA) and the U.K. Space Agency (UKSA). The mission will provide the first global survey of Earth's surface water and will observe the fine details of the ocean's surface topography, as well as how they change over time. This information is key to answering scientific questions on the kinetic energy of the ocean circulation and the global water cycle on land.

The unprecedented resolution and height measurement accuracy achieved with SWOT is enabled by a novel instrument called KaRIn. Conventional altimetry relies on the power and specific shape of the leading edge of the return waveform to retrieve height at the nadir point. The interferometric technique, in contrast, is based on measuring the relative delay between the signals acquired by two antennas separated by a known distance, referred to as baseline, together with range information. From that, one can derive the height for every imaged pixel in the scene.

The KaRIn instrument is complemented by the following suite of instruments:

1) a dual-frequency (C- and Ku-bands) NA, similar to the Poseidon altimeter flown on the Jason series;
2) a three-frequency swath microwave radiometer, similar to the advanced microwave radiometer (AMR) flown on the Jason series, but with two feeds each directed to opposing sides of the nadir track;

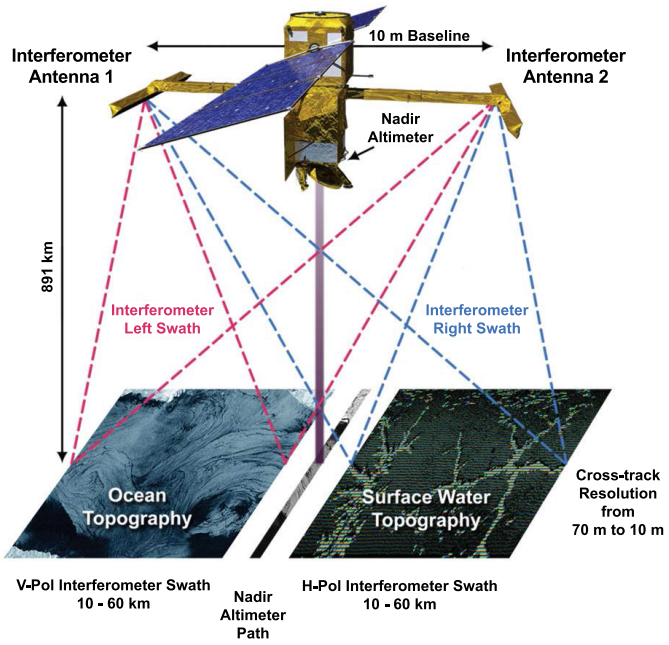

Fig. 1. Conceptual illustration of the KaRIn meausurement. KaRIn illuminates two swaths of 50 km and ±10–60 km on each side of the nadir track, and the nadir gap is covered by SWOT NA.

3) a DORIS receiver, a GPS receiver, and a laser retroreflector array (LRA) for POD.

The SWOT measurement covers a 120-km swath, with KaRIn providing data from 10 to 60 km on each side of the nadir track and the NA covering the 20-km gap along the nadir (Fig. 1).

SWOT was launched on December 16, 2022 onboard a SpaceX rocket from Vandenberg Space Force Base in California, into a one-day repeat orbit at an altitude of 857 km and an inclination of 77.6°. The checkout and commissioning phase was completed over approximately the first three months of this orbit and was followed by the calibration phase also approximately three months long. During checkout and commissioning, the S/C bus, ground systems, and instrument were fully characterized by the instrument teams. By the end of this phase, all S/C and instrument subsystems had been verified to be fully operational and to be within the on-orbit performance needed to begin the calibration phase. The main objective of the calibration phase was the calibration and initial validation of all instruments, as well as performance characterization of these same instruments. In addition to that and concurrently with calibration, this orbit also had a scientific objective: to understand the decorrelation times of the ocean mesoscale and submesoscale processes.

In July, the S/C transitioned to its final 21-day-repeat science orbit, with the instruments returning to operational mode on July 26, 2023, thus starting SWOT's three-year prime mission. SWOT's science orbit, a non-Sun-synchronous orbit at an altitude of 890.5 km and 77.6° inclination, was carefully selected to minimize the impact of tidal signals aliasing into the ocean topography data while still covering important polar ocean areas.

A. Ocean Science Key and Driving Requirements

In order to resolve submesoscale processes, centimetric accuracy is required for the ocean topography measurements. The ocean science requirement [12] has been separated into two different wavelength regions.

1) KaRIn provides the fundamental topographic measurement at wavelengths shorter than 1000 km as a swath measurement.
2) The NA covers the wavelengths larger than 1000 km as a nadir-only measurement.

Since the NA measurement boasts substantial heritage [13], [14], we will focus this article on KaRIn, the novel instrument that greatly expands the science possibilities demonstrated by earlier altimetry missions.

Measurement of mesoscale and submesoscale ocean topography requires that the measurement noise will be, ideally, one order of magnitude smaller than the signal. Since the signal level changes with wavelength, the SWOT error requirement for wavelengths shorter than 1000 km is expressed as a PSD. Before SWOT's launch, there was only limited information about the ocean topography for wavelengths less than 100 km. A global estimated spectrum of the SSHA[1] was estimated from Jason-1 and Jason-2 observations,[2] and is illustrated in Fig. 2. The SSHA error spectrum requirement (in red) was defined so as to achieve 10-dB SNR for wavelengths longer than 100 km with a probability greater than 68% and is expressed analytically as follows:

$$E(f) = 2 + 0.00125\, f_{\mathrm{oc}}^{-2} \ \left[\mathrm{cm}^2/\mathrm{cpkm}\right] \qquad 1/15 \ \mathrm{cpkm} > f_{\mathrm{oc}} > 1/1000 \ \mathrm{cpkm} \quad (1)$$

where f_{oc} is the ocean wavenumber in cycles per kilometer (cpkm). The SWOT ocean requirement has to be met for an SWH less than 2 m, which is the same requirement levied on the NA.

Because KaRIN makes a 2-D measurement, this requirement is defined as the cross-track average of the along-track spectra computed at different cross-track locations over the swath after averaging in cross track to 7.5-km pixels, the Nyquist limit sufficient to resolve a 15-km wavelength.

Equation (1) consists of two parts: a constant white noise contribution of 2 cm^2/cpkm, which dominates at small wavelengths, and a correlated noise contribution, dominates at longer wavelengths, and represents residual geophysical, orbit determination and media errors, and, most importantly, KaRIn systematic errors [15]. Many of these errors, including KaRIn's systematic errors, are not isotropic. In the cross-track direction, KaRIn's systematic error appears predominantly as a linear error, together with small bias and quadratic components, all of which drift is along track. In addition, there is a residual differential phase screen that creates a small height error in cross track that evolves slowly with orbital and seasonal variations (see Section III-E).

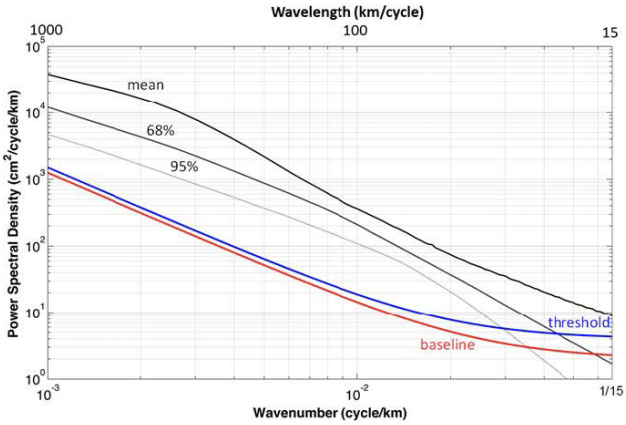

Fig. 2. SSHA spectrum requirement as a function of wavenumber. The red curve is the baseline requirement, which forms the basis for the implementation plan. The blue curve is the threshold requirement, which establishes the minimum success criteria beyond which the fundamental science value of the mission would be impacted. Shown, for reference, is the global mean SSHA spectrum estimated from the Jason-1 and Jason-2 observations (black thick line), the lower boundary of 68% of the spectral values (the upper gray dotted line), and the lower boundary of 95% of the spectral values (the lower gray dotted line).

The SWOT measurement resolution is defined to be the intersection of the signal with the error spectrum, which occurs at about 15 km (68%) and 25 km (95%). The threshold requirement was set at resolving approximately 20-km wavelengths or, equivalently, at a noise threshold of 4 cm^2/cpkm. Finally, the mission had a goal[3] to achieve a noise level of 1 cm^2/cpkm.

B. Hydrology Science Key and Driving Requirements

SWOT's primary hydrology science objective is to improve our understanding of the global water cycle by producing measurements of the spatial and temporal variability in surface water storage and discharge. The key hydrology performance requirements [12] are given as follows.

1) The nonvegetated area of all water bodies greater than 250 × 250 m and rivers wider than 100 m must be measured with a relative error less than 15% (1-sigma) of the total water body area.
2) The vertical precision of water surface elevation (WSE) measurements averaged over a nonvegetated area of 1 km^2 (lake, reservoir, wetland, and river) must not exceed 10 cm (1-sigma).
3) The river slopes for river widths wider than 100 m must be measured to an accuracy of 17 μrad (1.7 cm/km) after averaging no more than 10 km downstream the river.

These highly stringent requirements can only be met with the KaRIn instrument. However, contrary to oceanography, in which KaRIn's performance only needs to be met over 1000 km or, equivalently, about 3 min, in order to meet the hydrology requirements, instrument drifts between subsequent measurements need to be removed. This requires the use of

[1]The SSH is defined as the SSH measurement above the ellipsoid. The SSHA is calculated by subtracting from the SSH the contributions from the mean sea surface, tides, and the high-frequency response to atmospheric forcing from the SSH measurement.

[2]Data from other NA missions are now available, such as Sentinel 3A-3B, Jason-3, and AltiKa, and are being used as part of SWOT's validation campaign.

[3]The KaRIn instrument was designed to meet the baseline requirements, but science goals were tracked and used by the engineering team to inform trades and apply resources.

calibration techniques such as crossover calibration [16]. However, for this technique to work, we need to impose additional requirements on KaRIn at longer wavelengths, as will be explained in Section III.

C. SWOT Mission Error Budget

The SWOT mission error budget and how the various error sources are suballocated is thoroughly explained in [15] and [7]. Here, we will summarize the main errors to provide context for future sections, focusing on the ocean wavelength region <1000 km and on the hydrology requirements, both of which directly impact KaRIn.

In general, the error sources can be classified as random, systematic, media, orbit, or motion errors. Over the ocean (and very large water bodies such as the Great Lakes), there are also wave-related errors. From these, only the first two—random and systematic—are part of KaRIn error budget. The overall SWOT performance, including all error sources, is currently being validated as part of SWOT's validation campaign.

1) Random Errors: These are errors that are independent of pixel-to-pixel, which cannot be removed through the use of techniques such as tie points [17] or crossover calibration [16]. They can potentially be reduced by averaging at the expense of resolution. This error source is fully allocated to KaRIn and will be discussed in Section III-F.

2) Systematic Errors: These are nondestructive errors typically associated with drifts, mostly in differential phase and range, that introduce slowly varying biases in the measured heights. A portion of this error is suballocated to S/C disturbances, but the large majority is suballocated to KaRIn and will be described in Section III-E. The KaRIn system has been designed with a first mode requirement larger than 7 Hz, which ensures that any dynamic disturbances are not amplified below 6.5 Hz, corresponding to a 1-km ocean wavelength.

3) Electromagnetic Propagation (Media) Errors: The ranges measured onboard by the interferometer must be corrected to account for additional delays caused by propagation effects through the ionosphere and troposphere.

4) Orbit Determination Errors: Errors in the knowledge of KaRIn radial position directly translate into height errors. The POD suite of instruments is used to correct these errors.

5) Motion Errors: It is well known that for an SAR [18], [19], an unknown motion of the ground target will cause an apparent shift of its location in the SAR imagery, which translates into an error in the retrieved heights. This error was estimated to be negligible for SWOT [15] and we revisit that in Section VI-E.

6) Wave Related Errors: These include the SSB, also known as electromagnetic (EM) bias.

7) Algorithm Errors: The ocean product has a phase bias that needs to be corrected on the ground. Errors in computing that phase bias correction are suballocated between algorithms and the KaRIn instrument, as discussed in Section III-E.

For hydrology, a large portion of the error is due to limitations in correcting KaRIn's long-term drift, which is performed by crossover calibration [16]. In addition, there will be errors due to, for example, topography (layover, shadowing, and islands), vegetation, classification errors, phase unwrapping errors, and abnormal phenomenology (such as regions of still water with very low reflectivity over the swath) that will impact the hydrology performance [5]. Since these are the dominant sources of hydrology error, most of the discussion in this article is focused on the ocean requirements.

TABLE I
KARIN KEY SYSTEM PARAMETERS

Parameter	Value
Center frequency	35.75 GHz
TX Bandwidth	200 MHz
TX Pulse length	6.4 us
Pulse Repetition Frequency	4,420 Hz per swath
Peak Transmit Power	1,500 W (end of life)
Physical Baseline Length	10 m
Antenna size	5 m x 0.26 m
Boresight Look Angle	+/- 2.65 deg
Polarization	Right Swath VV, Left Swath HH

III. KARIN: THE KA-BAND RADAR INTERFEROMETER

In this section, we will describe the KaRIn radar key and driving requirements, the radar architecture that was selected to meet those requirements, and the unique OBP that allows for a substantial reduction in the downlink data rate. Finally, we will describe the high-level suballocation of random and systematic errors.

A. KaRIn Radar Overview

KaRIn is an SAR interferometer operating at Ka-band (35.75-GHz center frequency). KaRIn advances the state-of-the-art in several aspects, including the deployment of the largest reflectarray antenna ever flown in space [20], an HPA with unprecedented stability requirements [21], a large deployable 10-m boom with stringent alignment and thermoelastic deformation requirements, and the first-ever onboard processor that, ingesting massive amounts of data, produces radar interferograms on board an S/C.

The key system parameters are summarized in Table I. The antenna subsystem is formed of two 5-m-long and 0.26-m-wide deployable antennas on opposite ends of a 10-m boom, which forms the interferometric baseline. The antenna employs printed reflectarray technology, consisting of a flat reflectarray aperture with etched Ka-band patch elements on its surface providing the phase change required to emulate a parabolic reflector [22]. This architecture enables stowage of the antenna to fit inside the launcher fairing.

KaRIn operates in a mode commonly known as "single transmit antenna" (Fig. 3). One of the antennas transmits the radar 6.4-μs pulse, a linearly frequency-modulated (i.e., chirp) pulse, and both antennas simultaneously receive the radar echoes. The interferometer alternatingly illuminates the swaths left and right of the nadir track with a nominal pulse repetition frequency (PRF) of 4.42 kHz per swath. This is accomplished by two waveguide-fed horn feed antennas per reflectarray antenna operating with orthogonal linear polarizations

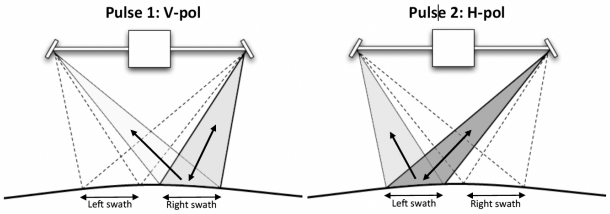

Fig. 3. KaRIn alternates illumination of left and right swaths on each side of the track. One antenna transmits the pulse and both antennas simultaneously receive the radar echoes.

(V and H polarizations), which enable each antenna to generate two separate beams scanned $\pm 2.65°$ off boresight, one at each polarization.

The instrument's spatial resolution in the direction parallel to the baseline direction (across the swath) is determined by the system bandwidth. With a 200-MHz transmit bandwidth, KaRIn achieves ground resolutions in the cross-track direction ranging from approximately 70 m at the near edge of the swath down to 10 m at the far end of the swath, which is sufficient to meet the hydrology requirement of resolving 100-m-wide rivers.

As an SAR [18], [19], the spatial resolution in the along-track direction (perpendicular to the baseline direction) is given by the length of the synthetic aperture that can be realized. The highest theoretical resolution that can be obtained is approximately half the antenna length or 2.5 m. In practice, the resolution is determined by a combination of factors, including the antenna pattern, the processed azimuth bandwidth, and the scene decorrelation time.

The novelty of KaRIn, the key feature that enables its unprecedented accuracy, is that KaRIn is an SAR interferometer [7], [8]. The interferometric concept is illustrated in Fig. 4, illustrating the relationship between the range measurement and the topography. For a given point on the ground, the difference between the distance of the two antennas, r_1 and r_2, is determined by the interferometric phase, Φ, given by the following equation:

$$\Phi = k(r_2 - r_1) \approx -kB\sin\theta \tag{2}$$

where θ is the look angle, $k = 2\pi/\lambda$ is the EM wavenumber, λ is the EM wavelength, and B is the baseline, i.e., separation between the antennas phase centers. From the interferometric phase measurement and with precise knowledge of the range distance from timing information, the elevation, h, above the reference plane (assuming flat Earth geometry) is obtained as

$$h \approx H - r\cos\theta \tag{3}$$

where H is the altitude of the platform, r is the range, and h is the surface height. It should be noted that (3) is just an approximation and is not used by the SWOT ground processing team to actually determine surface elevations.

B. KaRIn Key and Driving Requirements

The ocean PSD error requirement described in Section II-A and (1) is a major driver for KaRIn's performance requirements. The error budget assumes that the various error sources described in Section II-C are uncorrelated and their PSDs

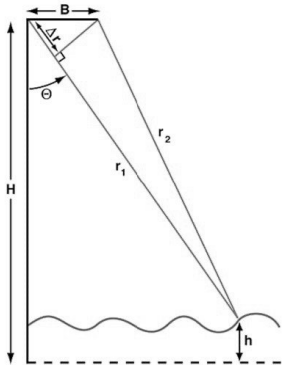

Fig. 4. Interferometric measurement concept. The range is determined by the system timing accuracy and the range difference between the signals acquired by the two antennas is obtained from the interferometric phase [15].

can be linearly added. The PSD for media, POD, motion, wave, and algorithm errors was bounded based on models and simulations [15]. The majority of the residual error was allocated to KaRIn based on the instrument's capabilities, with a small fraction remaining as a margin.

In addition, KaRIn's stability by itself is not sufficient to meet the hydrology requirements, and it requires the use of ground algorithms such as the crossover calibration to remove long wavelength drifts. In order to decouple KaRIn's requirements from the ground algorithm performance, the KaRIn PSD requirement in (4) was extended to wavelengths of 12 500 km. In addition, global RMS requirements are imposed on roll, differential phase, timing, and baseline dilation. Together, these requirements are sufficient to reach the required crossover hydrology performance, as validated by analysis and confirmed through simulation. Our French colleagues independently verified this analysis using realistic simulated KaRIn data [16].

The resulting KaRIn PSD requirement in cm^2/cpkm is as follows:

$$\begin{aligned} E_{\mathrm{KaRIn}}(f_{\mathrm{oc}}) &= 1.89 + 3.6153 \times 10^{-4} f_{\mathrm{oc}}^{-2} \\ &\quad + 1.3236 \times 10^{-5} f_{\mathrm{oc}}^{-2.5} \\ 1 \text{ cpkm} > f_{\mathrm{oc}} &> 1/12\,500 \text{ cpkm}. \end{aligned} \tag{4}$$

This requirement presumes atmospheric absorption not exceeding 1 dB and ocean backscatter that follows the Vandemark-2004 model [23] with an 8.9-m/s wind speed (68% percentile). Any uncertainty in the phenomenology is not part of the KaRIn instrument requirement and is carried out at a higher level.

The white noise allocated to KaRIn is 1.89 cm^2/cpkm, which translates into a height error of 2.7 cm for a 1-km^2 pixel. Hydrology requirements do not drive the SNR requirement. Although the onboard presuming (performed to reduce the data rate as described in Section III-D2) degrades the random performance slightly, the hydrology height and slope requirements are still met given the ocean SNR requirement.

C. KaRIn Radar Hardware Architecture

The KaRIn instrument consists of two reflectarray antennas separated by a deployable mast, with feeds and KaRIn electronics mounted to a metering structure located inside the

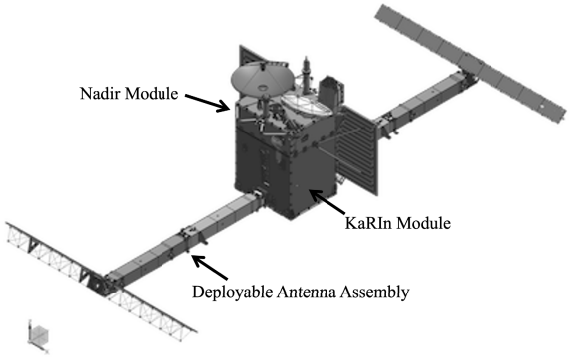

Fig. 5. SWOT observatory overview.

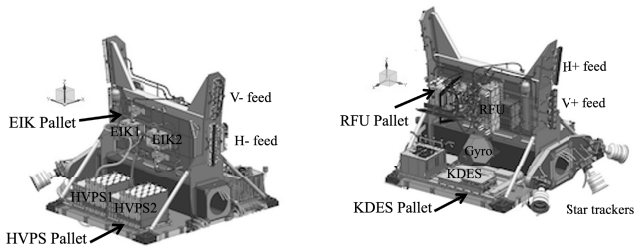

(a) (b)

Fig. 6. Two views of the KaRIn module, with the KaRIn electronics and feeds mounted on the metering structure. (a) View of HVPS and EIK pallets. (b) View of RFU and KDES pallets.

KaRIn module (Figs. 5 and 6). The KaRIn module includes a CNES-provided RFU, a redundant HPA that contains a CSA-provided EIK powered by a Jet Propulsion Laboratory (JPL) high voltage power supply (HVPS), and the KDES with included FSW. The KaRIn mast, feeds, and waveguides are mechanically connected to the metering structure. The RFU and EIK, which connect via waveguides, are mounted to two separate "vertical" pallets on each side of the metering structure, and the HVPSs and KDES are mounted to the two "floor" pallets (see Fig. 6). KaRIn contains a high-performance fiber optic gyroscope IMU at the center of the metering structure to provide attitude information. Three star trackers are also mounted directly to the metering structure to minimize roll errors.

In order to achieve the key driving requirement of the radar, the thermal stability of the electronics is required in addition to mechanical stability and low thermoelastic variability. The thermal control system is composed of loop heat pipes (LHPs) that compensate for thermal changes in the environment in a slow and smooth manner. This is a self-adjusting thermal feedback system, which is assisted by S/C heaters to start and stop the heat transport from the thermal pallets to the radiator panels. The LHPs are switched off in the survival mode when the radar is off, isolating the pallets from the radiator in order to conserve survival heater power.

KDES is the "brain" of the radar. It contains the interfaces to receive platform position and time messages from the S/C bus as well as commands from the ground team. KDES sends telemetry and high-speed science data packets to the S/C, which stores them onboard until they are downlinked to the ground stations. In addition, KDES contains the four ADCs necessary to digitize the downconverted interferometric channels, it contains the FSW that performs all necessary computations based on uploaded onboard tables, and it reduces the data rate using OBP firmware. KDES also commands static parameters to the RF hardware, and it collects the health and status information to be downlinked in telemetry.

The RFU is composed of a hyperbox (Hx) contributed by CNES and a duplexer (Dx) contributed by the UKSA. The Hx provides the following functions:

1) chirp generation;
2) upconversion of the chirp into the Ka-band exciter input to the KaRIn HPA;
3) duplication of the exciter signal, sent into the Dx as a calibration loopback;
4) low-noise dual downconversion, for receiving the interferometric pair of radar echoes from the Dx and producing in-phase (I) and quadrature (Q) baseband signals that are sent to KDES;
5) generation of LOs for the Hx up and downconverters;
6) generation of synchronous radar clocks for KDES.

The Dx is a high-power Ka-band switch matrix for transmit/receive and calibration signal routing between antenna, EIK, and receivers.

The KaRIn HPA is a novel vacuum-tube amplifier (EIK) designed and built by CPI Canada. The EIK is a multicavity tube, and it efficiently amplifies the RF chirp coming from the RFU to output 1.5 kW of RF power with over 200-MHz bandwidth at the Ka-band. RF signal amplification is achieved by the conversion of kinetic energy of an electron beam into RF power.

The HVPS for the EIK, designed and built by JPL, is a complex assembly generating the thousands of volts required by the EIK and providing protections and sequencing for it.

A high-power filter and isolator assembly was developed for the output of the EIK in order to improve the RF match to the RFU Dx as well as to reduce the harmonics to comply with NTIA requirements.

Finally, in order to achieve the tight differential pointing requirements, KaRIn includes two alignment mechanisms, one for each reflectarray.

In the mission mode, when collecting science data, KaRIn draws an 800-W orbital average from the S/C bus. The KaRIn hardware mass is about 600 kg.

D. KaRIn Onboard Processing

The SWOT mission has a requirement to collect data over a minimum of 90% of all ocean and land areas covered by its orbit inclination, for 90% of the operation time. With a raw data rate of about 4 Gb/s, without including calibration products, the only way to achieve this is with substantial OBP to reduce the data rate.

KaRIn's OBP has two main products.

1) An LR product that is downlinked continuously and reduces the data rate to 13 Mb/s (about a factor of 310). It is primarily intended to be used over open ocean and

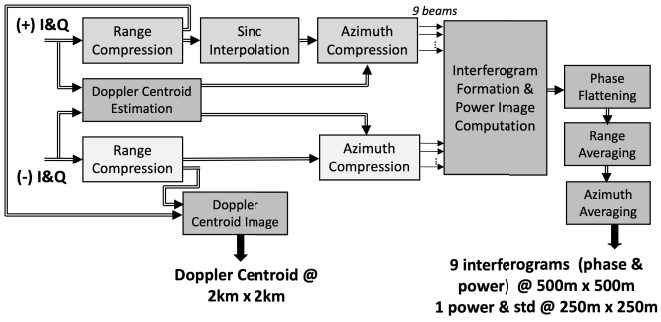

Fig. 7. LR OBP flow.

large surface water bodies but could potentially also be used over relatively flat ice.

2) An HR product that is downlinked only for certain regions, which are specified through a commendable onboard table and reduce the data rate to 317 Mb/s (about a factor of 13). It is the main product used for hydrology and can also be used over coastal areas.

In order to characterize KaRIn's OBP, we developed floating-point models for the FSW and the algorithm implemented in firmware, the so-called golden models. We also produced a fixed-point model for the firmware using the same word lengths, rounding, and truncation implemented in the hardware, referred to as the BTM. This BTM allowed us to compare the model output results directly with the hardware outputs and identify possible issues in the firmware implementation.

KaRIn also includes a debugging mode that allows us to collect about 0.75 s of raw ADC samples for one swath at a time. This was used during commissioning to verify the firmware and to assess the radar's point target response.

A detailed description of the OBP in KaRIn is outside the scope of this article and can be found in the corresponding algorithm theoretical description documents [24]. The following sections are intended to provide the reader with high-level information.

1) LR Onboard Processing: The LR OBP performs unfocused squinted Doppler-sharpened SAR processing, in which nine squinted beams are formed. The following products are produced:

1) a complex product of the two interferometric channels for each swath and beam, and power SAR images for each interferometric channel, swath, and beam, at approximately 500-m ground resolution and 250-m posting in both range and azimuth directions;
2) estimated Doppler centroid used for OBP;
3) average SAR image power and SAR image power variance (average of SAR image power squared) for the center beam of each swath at approximately 250-m ground resolution and 250-m posting;
4) Doppler centroid complex image for each swath at approximately 2-km resolution and 2-km posting.

The main processing steps are illustrated in Fig. 7. The reader is referred to the literature for further explanation on these steps (e.g., [18]). The fractional Doppler centroid is estimated using the pulse pair algorithm in the input raw

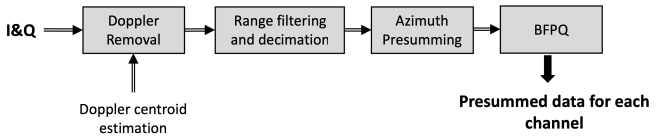

Fig. 8. HR OBP flow.

data. The data are range compressed using a stored reference function, which can be different for each channel and swath. Time co-registration between the channels is performed using sinc interpolation of the plus channel. The next step is Doppler sharpened unfocused SAR processing. Nine beams are formed by applying nine phase ramps and low-pass filters in time to a collection of nine pulses. The phase ramps are equally spaced in azimuth and include a phase term to remove the range-dependent Doppler centroid computed onboard, resulting in the beam peaks being separated about 200 m in the along-track direction.[4] The interferogram and power images are calculated and a phase ramp corresponding to a spherical surface approximating the Earth is removed before range and azimuth averaging to the desired resolution. The Doppler centroid complex image is computed from range compressed data.

2) HR Onboard Processing: Processing is applied to each channel of each swath independently. The processing steps are illustrated in Fig. 8.

First, the Doppler centroid, computed using a similar calculation to that used during the LR OBP but with an independent set of parameters, is removed. The data are then filtered and resampled in the range dimension to reduce the data rate by a factor of 2/3, utilizing the fact that the signal is sampled at 300 MHz but has a bandwidth of about 200 MHz. The data are subsequently presumed in the along-track direction, filtering the data and decimating it by a factor of either 2.125 or 2.4375. Finally, the data are compressed using a block floating-point quantization (BFPQ) algorithm [25] with 3-bit mantissa and 5-bit exponent.

3) KaRIn Flight Software: KaRIn FSW plays a fundamental role in KaRIn, well beyond just handling the communications with the S/C and the ground. The OBP algorithm is highly parameterized, with parameters stored in nonvolatile memory and passed by FSW to the OBP hardware. In addition, FSW dynamically calculates numerous parameters needed by the OBP and passes them to the OBP at precise timing boundaries. Some of these are computed from time-based onboard tables, including the PRF, which is adjusted over the orbit to ensure that the echo remains within the data window; the topography height; a correction to the Doppler centroid; and the downlink mask that determines whether the HR data will be downlinked. It also computes other parameters such as the data window position, which determines the start of the processing window, and the platform altitude, which is computed from a polynomial produced by DORIS.

Utilizing the fact that SWOT's track repeats to within ± 2 km of the reference orbit for all orbits, these tables are

[4]The nine beams are labeled in this article from -4 to $+4$, with beam 0 the most closely aligned with the antenna boresight and beam -4 the aftmost beam.

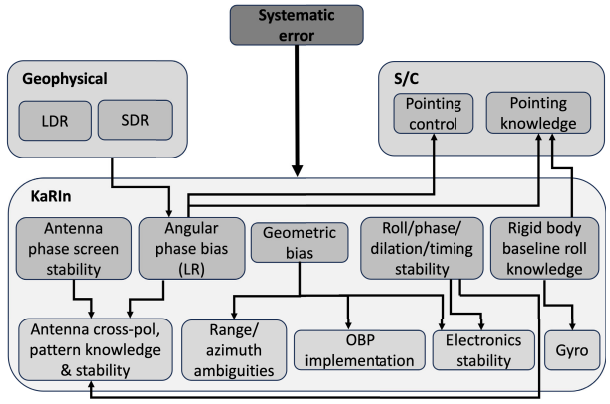

Fig. 9. Conceptual high-level flow down of the KaRIn systematic error to system elements.

constructed as a function of "table time," a time base following the reference orbit.

One of the most important KaRIn commands is the "URHere" command. This is sent first at turn-on, after new tables are uploaded, and also any time SWOT significantly deviates from the reference orbit due to, for example, collision avoidance maneuvers. This command contains the mapping between absolute time and table time at the future instant when the command is scheduled to be executed by the S/C and also contains the place in the tables where KaRIn will be at the time. From that, FSW computes corrections to table time every 10 s using latitude and longitude information from DORIS. This scheme greatly simplifies the algorithm, allowing FSW to "walk" through the tables without any interpolation or searching.

E. KaRIn Systematic Error Performance

A high-level flow of the systematic error key components is shown in Fig. 9 (see [15] for additional detail).

1) Baseline Roll: KaRIn systematic performance is largely dominated by baseline roll knowledge errors. A baseline roll knowledge error is equivalent to a look angle knowledge error and, through (2), an interferometric phase error. Baseline roll errors have the effect of creating a local tilt of the entire swath.

The main contributor to baseline roll errors is the S/C attitude. The KaRIn instrument, therefore, carries a high-performance gyroscope that will provide the required knowledge of the S/C rigid-body roll angle. This gyroscope is mounted to the same metering structure to which the mast and feeds are attached. This minimizes the second-largest source of KaRIn systematic error, which is roll error introduced by the thermoelastic distortions of the KaRIn mechanical system formed by the boom, antenna, and feed support structures, and is not measured by the gyro.

2) Differential Phase: A differential phase error can be introduced at any point in the RF chain. However, the largest contributors are the antennas, including feeds, and the high-power waveguides since these are the components that experience the largest temperature changes across orbits and beta angles.[5] Similar to roll, the impact on SSH error is approximately linear in cross track.

3) Baseline Dilation: Knowledge of the baseline length, defined as the distance between the antenna's phase centers, is needed to retrieve height. Drifts in the baseline length create an error that is quadratic across the swath.

4) System Timing: A system timing error introduces a height error that, given KaRIn's near-nadir geometry, is to first order a constant height bias.

5) Phase Screen Stability Error: Even though we like to think of systems in simple terms such as phase and group delay, the reality is usually more complex, and that is also true in the case of KaRIn thermoelastic distortion, especially regarding the antennas. As the feed, mast, and antenna reflectarray distort due to thermoelastic effects, the interferometric phase also changes shape in cross track.

During calibration, the calibration/validation (Cal/Val) team was able to successfully retrieve the largest part of what we call the phase screen, which compensates for our lack of pre-launch knowledge of the interferometric phase across the swath. This includes additional sources of scattering, such as the boom and S/C structures, which create what is known as multipath [26]. However, this phase screen is not completely static, especially when considered over the large range of temperatures experienced over different beta angles. Even though it is feasible to introduce a beta-dependent phase screen correction, the default assumption is that the correction is static and the remaining residual is captured as part of a KaRIn error.

6) Angular Phase Bias for LR: For SWOT's near-nadir geometry, the iso-range and iso-interferometric-phase lines diverge significantly within one resolution cell of the LR product. This misalignment introduces a systematic phase bias in the LR product (see [24] for a detailed discussion).

The systematic angular phase bias is a function of the backscatter, σ_0, spatial variability, pointing, the antenna patterns, the point target response of the system, the reference surface used to co-register the images, and the topography.

Errors attributable to the reference surface, topography, and the copolarization variability of σ_0 are considered algorithm errors since the instrument cannot do anything to reduce those, whereas they could be minimized at the cost of additional algorithm complexity.

The KaRIn instrument error budget assumes an ideal reconstruction of the phase bias on the ground but includes errors in the phase bias correction due to the following.

1) Attitude control and knowledge errors (dominated by pitch).
2) Antenna pattern knowledge errors.
3) Antenna cross polarization. The magnitude of this error is in turn impacted by the spatial variability of the following:
   a) LDR, $\sigma_{0\mathrm{HH}}/\sigma_{0\mathrm{HV}}$ or $\sigma_{0\mathrm{VV}}/\sigma_{0\mathrm{HV}}$;
   b) SDR, $\sigma_{0\mathrm{HH}}/\sigma_{0\mathrm{VV}}$.

7) Geometric Bias: The geometric bias includes various errors, such as range and azimuth ambiguities, channel isolation, drifts in the RF frequency centroid, and biases introduced

[5]In this article, we define beta as the angle between the solar vector and its projection onto the orbit plane.

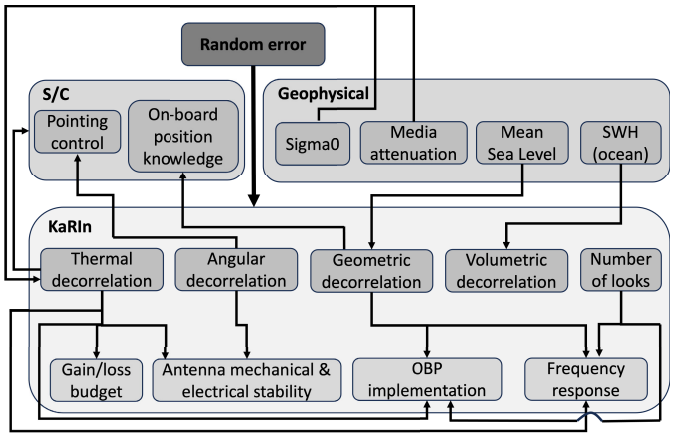

Fig. 10. Conceptual high-level flow down of the KaRIn interferometric phase random error to system elements.

by the algorithm or its fixed-point implementation. KaRIn is designed to minimize these errors.

F. KaRIn Random Error Performance

For a rigorous derivation of decorrelation and random height error, the reader is referred to [27] and [28]. Here, we describe a simplified approach that shows that the interferometric random error is a function of the interferometric phase standard deviation, $\Delta\Phi$, baseline, wavelength, swath extent, and platform altitude as follows:

$$\Delta h \approx \frac{C}{kB}\Delta\Phi\left(1+\frac{H}{R_E}\right) \tag{5}$$

where C is the cross-track distance and R_E is the Earth radius.

The phase standard deviation is in turn related to the number of independent looks that are averaged, N_L, and the signal decorrelation, γ, through the following expression [7]:

$$\Delta\Phi^2 = \frac{1}{2N_L}\frac{1-\gamma^2}{\gamma^2}. \tag{6}$$

Note that (6) is not valid for a small number of looks, and the phase standard deviation approaches this limit asymptotically as the number of looks increases. However, for most systems, including KaRIn, a large number of looks are typically used.

A high-level flow of the interferometric phase random error key components is shown in Fig. 10. The signal decorrelation is driven by the SNR and the baseline length. The dominant decorrelation sources are thermal, γ_N, geometric, γ_G, and volumetric, γ_V. Smaller decorrelation sources are angular, γ_A, dynamic, γ_D, and due to the I/Q modulation scheme, γ_{IQ}. The total decorrelation, γ is given by the product of all the decorrelation sources

$$\gamma = \gamma_N\gamma_G\gamma_V\gamma_A\gamma_D\gamma_{IQ}. \tag{7}$$

Over the ocean, there is an additional error source that spectrally appears to be random, but it is not due to decorrelation. This is the nonlinear wave effect described in [29].

In addition, looks can be lost by filtering in the range or Doppler spectra, which also leads to reduced bandwidth and degraded resolution.

1) Thermal Decorrelation: The thermal decorrelation is responsible for the most significant fraction of KaRIn's random error. The thermal decorrelation is a function of the SNR as follows:

$$\gamma_N = \frac{1}{1+\mathrm{SNR}^{-1}}. \tag{8}$$

The gain/loss budget drives transmit power, transmit pulsewidth, antenna gain, receiver noise, RF front-end losses, and noise bandwidth. Other sources of SNR loss are RF flatness, Doppler centroid estimation error, and antenna differential pointing.

2) Geometric Decorrelation: The main contributor to the geometric decorrelation is residual mis-registrations between the two images. However, we also include as part of this suballocation errors in the spectral filtering implemented in the onboard processor and spectral distortions in the transmit/receive response of the system.

3) Dynamic Decorrelation: There is uncertainty in the values used for platform and topography height used in the onboard processor. This introduces a small decorrelation term that increases in the near range.

4) Image Decorrelation: As explained in Section III-C, KaRIn uses an I/Q modulation and demodulation scheme. As a consequence of the nonidealities of the I/Q mixer [30], there is a residual LO leakage as well as an image of the signal, both of which introduce decorrelation. The image has the same frequency extent as the main signal, but the opposite chirp slope, so it does not compress during range compression. If I is the power of the image, S is the signal power, and N is the thermal noise power, the decorrelation is given by

$$\gamma_{IQ} = \frac{1}{1+\frac{I}{S+N}}. \tag{9}$$

For KaRIn's LR OBP, the ratio of image to signal is beam and Doppler frequency dependent.

5) Angular Decorrelation: The interferometric fringes vary over the azimuth cell, introducing an additional (yet small) amount of decorrelation, larger in the near range. This is especially important for the low-resolution OBP mode (Section III-D1), in which the azimuth resolution is significantly larger than the theoretical 2.5 m.

6) Volumetric Decorrelation: The ocean waves create a distribution of scatterers of varying heights within a range resolution cell, thereby introducing volumetric decorrelation that increases significantly in the near range and at high SWH.

IV. KaRIn Pre-Launch Performance Verification

KaRIn is a highly complex instrument, and it is not feasible to assess KaRIn's end-to-end performance only by measurement. The approach we took is a combination of models that feed into each other and that are validated and/or refined by measurement data.

The process is illustrated in Fig. 11.

1) Transient thermal analysis results produced using a system-level thermal model are mapped to a structural finite-element model (FEM; including antenna and

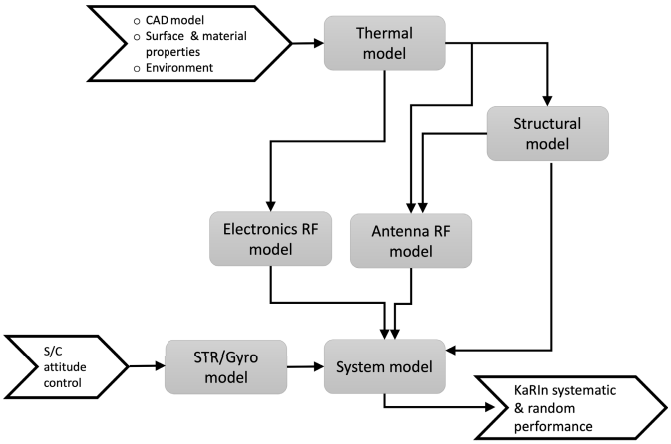

Fig. 11. KaRIn pre-launch performance assessment flow diagram. Thermal transient analysis results are used to compute thermoelastic deformations at relevant structural elements. These are fed into the antenna and the electronics RF model, whose outputs, together with the attitude control and knowledge simulation from a star tracker and gyro model, are used by the system model to evaluate random and systematic performance.

feeds). The thermal simulation is performed for an orbital period at several beta angles.

2) Thermally induced deformations at relevant RF and structural elements are assessed using a structural model.
3) The thermal predictions and structural deformation of the feeds and antenna panels are fed into the antenna RF model.
    a) First, the effective antenna panel translation and rotation for each of the two antennas is computed by finding the best-fit rigid-body translation and rotation that transforms the nominal antenna panel node locations into distorted node locations. This is used to compute an estimate of the baseline orientation, the antenna path length, and the antenna pointing.
    b) A high-fidelity model computes the complex dispersive RF antenna patterns at each time step. This serves as validation of the previously computed baseline and antenna phase and pointing, but it also provides insight into additional higher order effects such as group delay, antenna beamwidth, sidelobes, antenna phase across the swath, and RF frequency distortion.
4) The thermal results are also used together with electronics temperature sensitivities to obtain group delay and differential phase drifts.
5) Finally, an interferometric system model combines these results together with the attitude control and reconstructed knowledge error from a star tracker and gyro model to assess performance.

In addition to baseline performance predictions, this process enables performing sensitivity studies to assess the impact of modeling uncertainties, as well as to determine the contribution of each subsystem/element to the overall performance.

The following sections describe each of these models in more detail.

A. Thermal Model

The thermal model uses as inputs the S/C and payload CAD model, the material and surface optical properties, and the environmental loads (e.g. solar, albedo, and Earth infrared radiation). The model generated in NX Space Systems Thermal has a total of 53 060 elements, of which 23 840 are in the KaRIn payload and 17 580 are in the mast and reflectarray structures. This high level of fidelity is needed because of the tight stability requirements and in order to capture small shadowing features. The full system-level thermal model maintains synchronization with actual geometry to accurately model shadowing. A quasi-steady state is assumed, which means that the beta angle is assumed not to change over a single orbit (the change is less than 0.1° per orbit, so this is a reasonable assumption). The thermal environment assumes operation during SWOT science orbit with a maximum eclipse duration of 35 min and no eclipse for betas between 65° and 90°. There is a yaw flip when crossing beta 0° to keep the radiator panels facing away from the Sun. The model was run from 0° to +90° since the yaw flip results in the same effective thermal environment for 0° to −90°. Model sensitivities were performed to determine relevant orbital calculation and model integration times sufficient to capture thermal disturbances.

B. Structural Model

The SWOT satellite is modeled structurally as a mesh of finite elements using a finite element analysis (see [31], [32]). Specific points on the FEM at which simulation results are given are called nodes, which are usually located at the vertices of the polyhedral finite elements. Each reflectarray antenna consists of nine panels and each panel is modeled with 45 nodes. In addition, there is a node located at the nominal phase center of each of the four feeds. For each reflectarray node, we compute a time series of nodal translation along each of three axes for an orbital period at each beta angle of interest, with time spacing less than 20 s (the simulation is more closely spaced near the beginning and/or end of eclipses since thermal snaps cause faster changes in distortion). For the feed nodes, we also compute the nodal rotation along the three axes.

C. Antenna RF Model

The feed and antenna panel nodes from the structural model are used to assess the impact of thermoelastic structural distortion on antenna pointing, interferometric baseline, interferometric phase, and group delay.

We have developed two methods for this. The first method, referred to as the “linear” model, is based on sensitivities. It is computationally efficient and provides a first-order estimate of KaRIn’s performance. Most importantly, it provides physical insight into which factors are most critical for KaRIn’s performance and guidance to set subsystem mechanical requirements. The second method is a high-fidelity EM model based on the method of moments to compute the antenna patterns.

1) Linear Antenna RF Model: Using the methodology described in the Appendix, we compute the best-fit translations and rotations for each of the two antenna reflectarrays at each time step and beta angle. Then, we define the following:

1) effective baseline as the vector connecting the geometric centers for the two antennas;
2) path length as four vectors connecting each of the feeds to the geometric centers of the antennas.

From the effective baseline, we compute the roll and baseline dilation as a function of time and beta angle. From the path length, we compute the interferometric phase.

The dominant phase-error term is the differential phase drift in the feeds because of the wide range of temperatures experienced by the feeds on the side of the S/C facing the Sun over the beta angles. The feed phase dependence on temperature has been modeled (see Section IV-C2) and can be approximated as

$$\phi_{\text{feed}_i}(t) = -0.343\ \Delta T_{\text{feed}_i}(t) \tag{10}$$

where ϕ_{feed_i} is the phase for feed i and ΔT_{feed_i} is the change in feed average temperature relative to the ambient temperature.

KaRIn also has strict pointing requirements. Differential pointing, as well as elevation pointing to a lesser extent, directly impacts SNR. In addition to that, pointing errors impact the angular phase bias, ground algorithm performance, and angular decorrelation.

Pointing can be evaluated using our linear model analysis through the computation of sensitivities based on the antenna EM model (see Section IV-C2). Each of the two reflectarrays and four feeds is moved along each of six degrees of freedom (DOFs), i.e., three rotations and three translations, and antenna patterns are produced per DOF. The simulated antenna patterns are used to determine pointing sensitivities to each DOF. We define pointing in the native antenna pattern frame as a shift in azimuth and elevation and a rotation of the beam about boresight relative to the nominal patterns.

We also used these antenna patterns per DOF to understand the impact of thermoelastic distortions on the interferometric phase screen. As discussed in Section VI, this will be useful in understanding some of the flight observations.

2) EM Antenna RF Model: Using feed and reflectarray temperature as well as structural deformations, we simulated the orbital variation of the KaRIn antenna patterns, generated for each antenna per time step and at 11 frequency points in the chirp bandwidth.

For the EM model, we assumed that any one feed structure is at a homogeneous temperature (we assessed the impact of thermal gradients and determined that it is a higher order effect). The feed structure expands and contracts over temperature following the thermal characteristics of aluminum 6061 (AL6061). The variation in dimensions of the feed over temperature is equivalent to frequency shifts given by

$$\frac{df}{f_0} \approx -\frac{d\lambda}{\lambda} = -\frac{dl}{l} = -\alpha_L \Delta T \tag{11}$$

where f_0 is the nominal KaRIn center frequency, α_L is the AL6061 thermal expansion coefficient, and ΔT is the change in feed temperature. Feed patterns are calculated in HFSS [33] at ambient temperature over a set of discrete frequencies prior to orbital analysis. These patterns are then interpolated to the instantaneous frequency, $f_\alpha(t)$, which is given by

$$f_\alpha(t) \approx f_0(1 - \alpha_L \Delta T(t)) \tag{12}$$

where $\Delta T(t)$ is the average feed temperature change over the orbit relative to the ambient temperature.

The pattern at f_α and ambient temperature is used to represent the pattern at f_0 and temperature $T + \Delta T$. The coefficients of a spherical wave expansion at frequency f_0 at $T + \Delta T$ are used as inputs to REFANA, a JPL proprietary software package used to analyze reflectarray patterns using the method of moments and based on the Floquet mode unit-cell technique [20], [34], [35], [36]. Furthermore, each feed is translated and rotated given the distortions provided by the structural simulations.

Each reflectarray consists of nine panels, each with 132×62 patches. The reflection coefficient for each of the 73 656 patches is computed for the four feeds and 11 frequencies at nominal locations. Panel deformation data (45 nodes per panel) are interpolated to each of the 8184 patches per panel and used to displace each patch in 3-D space. The modified geometry file is then input to the REFANA software that uses the nominal reflection coefficient file to compute the distorted pattern. This is repeated for each frequency per time step per beta angle. Because of the extensive computation time, antenna patterns were generated for a subset of five beta angles from 0° to 90° sampled every 20 s.

For each 3-D antenna pattern, pointing is estimated as described in Section IV-C1. We also compute differential phase and group delay by integrating the antenna patterns over the beamwidth. Antenna group delay is defined as the derivative of antenna pattern phase over frequency. The differential phase is evaluated as the mean over frequency.

Fig. 12 shows a comparison of differential azimuth pointing and differential phase computed with the linear and EM models. The agreement between the two methods is fairly good, with both capturing similar orbital time and beta dependence. Accurate evaluation of other antenna parameters, such as group delay, phase screen, beamwidth, and sidelobes, requires the use of the full EM model.

D. Attitude Reconstruction Model

The rigid-body roll knowledge error is the largest systematic error contribution in KaRIn, and it was, therefore, crucial to develop a comprehensive model of attitude reconstruction performance. A sophisticated tool was created to simulate the inputs to the attitude estimator that included the star tracker's noise equivalent angle and low-frequency error, and the gyro's angle random walk, rate random walk, bias and scale factor stability, and nonlinear effects. It also includes misalignments between star trackers and gyros.

The input to this tool was the S/C inertial position and velocity, the target attitude and rate quaternions, and the real attitude and rate quaternions. These were produced by our CNES colleagues using their attitude and orbit control system simulator.

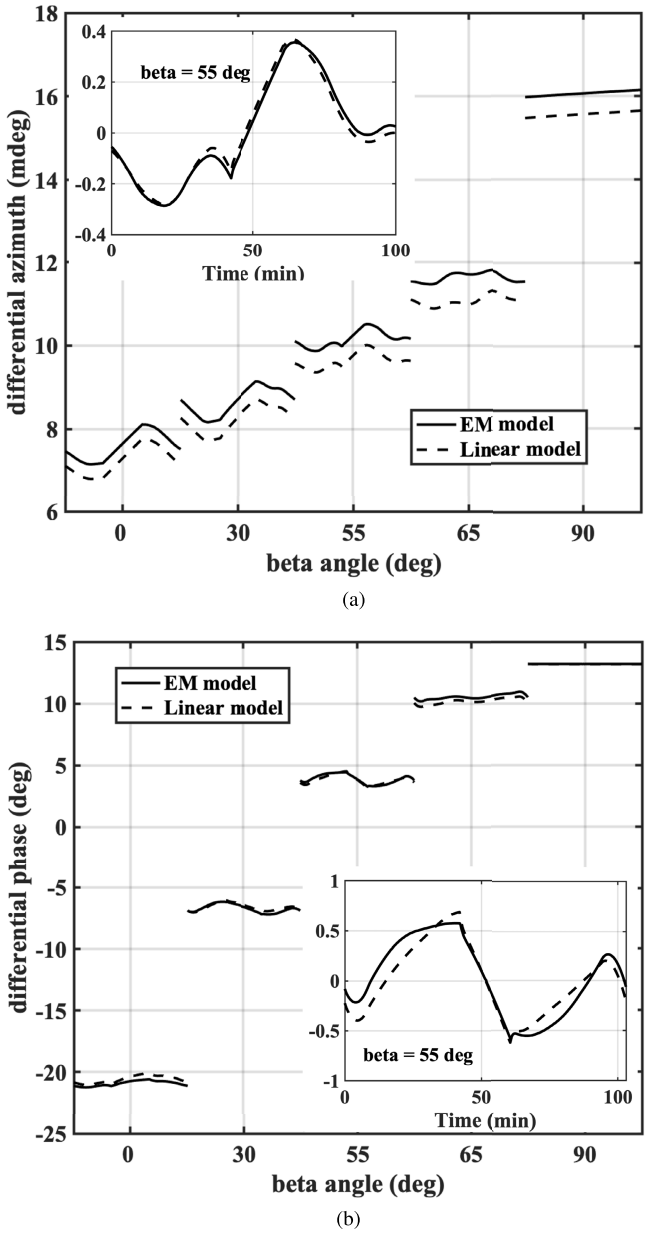

Fig. 12. (a) Differential azimuth pointing and (b) differential phase for V swath (H swath is similar). Each curve corresponds to the orbital variation for a beta angle (indicated in the x-axis) with solid line using the EM model and dashed line using the linear model. The inset zooms in the data at beta 55 as a function of orbital time after removing the mean value. This illustrates the ability of the simple linear model to accurately predict two of the most critical KaRIn error sources.

Shortly after turn on, a gyro calibration was performed to produce estimates for the gyro's biases, scale factors, and misalignments. Our pre-launch simulations included both the calibration sequence and the attitude estimation during nominal operations.

E. Electronics RF Model

The thermal model estimates temperatures of all relevant electronic boxes, which can be used to obtain phase, group delay, gain and noise at each time step, and beta angle by using the sensitivities of the various RF subsystems.

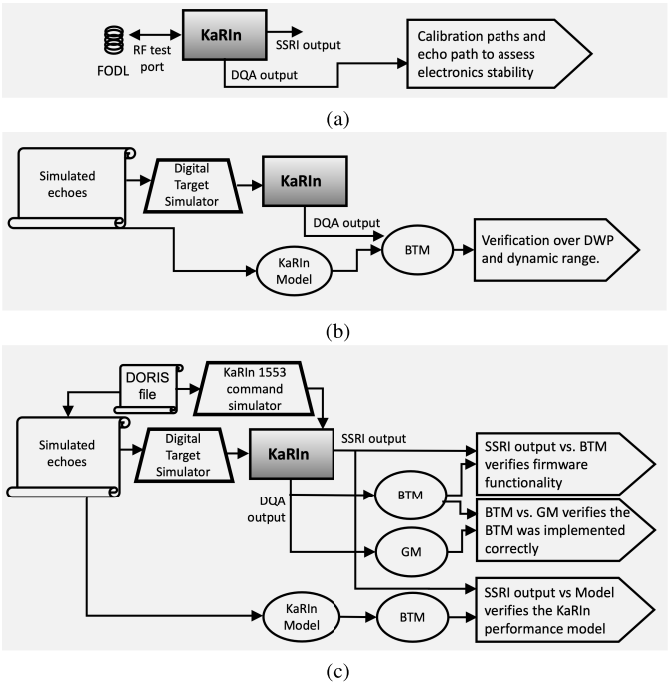

Fig. 13. KaRIn RF electronics performance and functional verification. (a) FODL test. (b) Equatorial target test. (c) Distributed target test.

In order to measure the sensitivity of the RF electronics, we use an FODL test, as illustrated in Fig. 13(a). In the FODL test, a sample of the transmit chirp is delayed by an FODL and injected back into the transmitter. This is the only test in which the signal produced by the transmit electronics is injected back into the receiver and measured during the receive window, and it is used to perform the most detailed stability performance verification. The digital samples measured by the KaRIn ADCs for the FODL signal together with the internal calibration signals are recorded using KaRIN's DQA output port. Using range compression, we compute the phase and group delay for each of the paths and compute sensitivities as a function of temperature. We can also perform simultaneous measurements of noise and gain.

In addition to systematic drifts that are temperature driven and typically slow, the KaRIn RF electronics exhibit a $1/f$ noise that impacts the higher frequency part of the spectrum, becoming, if uncorrected by calibration, a dominant systematic error source at wavelengths shorter than about 25 km. The FODL test characterizes this $1/f$ noise as well as our ability to remove it using the internal calibration signals.

The FODL test is, nevertheless, insufficient to verify end-to-end performance.

1) The injected signal is a chirp (equivalent to an ideal point target), not a realistic distributed target echo.
2) The injected echo is at a fixed delay corresponding to the FODL delay.
3) The injected pulses are identical for both plus and minus channels.
4) The FODL introduces a significant amount of group delay drift and noise common to both interferometric channels.

5) KaRIn cannot be operated using flight tables due to having to use a fixed data window position to match the FODL delay.

To address deficiencies 1–4, we designed what we called the equatorial target test illustrated in Fig. 13(b). For this test, we simulated the raw echo targets that KaRIn would receive in a highly idealized zero-inclination orbit over a zero-topography elliptical Earth. This scene is static from pulse to pulse and allows us to evaluate the random and systematic phase-error performance as settings are varied, including dynamic range, bus voltage, and data window position. As a reference transmit pulse for the simulated echoes, we used the measured transmit chirp, which has nonidealities such as amplitude/phase distortions and a dc offset that extends beyond the chirp duration. In order to evaluate the land performance, we also included idealized lakes (i.e., areas of higher reflectivity relative to the background) of various sizes and at different cross-track distances. These distributed target simulated data are upconverted using the DTS, which uses the same modulation scheme as KaRIn and the LOs from KaRIn test ports. Then, the echo signal at Ka-band is injected into the KaRIn RF test port. KaRIn OBP outputs cannot be used to analyze these data since this is still not a true flight signal, so instead, we used the ADC samples captured through the DQA and applied the BTM to assess the performance.

An important aspect of this test was to evaluate the signal correlation. As explained in Section III-F2, part of the decorrelation is due to the RF electronics filtering, IQ image, and LO leakage.

The decorrelation due to the transmit chirp, γ_{tx}, can be first assessed analytically by comparing raw data simulations using an ideal transmit chirp with those using the same parameters but with the measured transmit chirp. By comparing the correlation from raw data simulations to the measured correlation using the equatorial target test, we have empirically derived an additional receiver electronics decorrelation term, γ_{rx}. Even though we tried to make our test equipment as ideal as possible, the measured electronics decorrelation was assumed to be conservative, and this was confirmed with flight data (Section VI-B). The test equipment is at most as good as the flight hardware, and we cannot differentiate the decorrelation arising from the instrument versus the test equipment.

Using the equatorial target test data, we also check the validity of the SNR gain/loss budget with distributed targets.

Another important contributor to the systematic error is waveguides that are not captured by the RF test ports, for example, those connecting the electronics and the antenna feeds. Since we could not measure the temperature sensitivity of each waveguide, we instead built a sample flight-like stainless steel waveguide, on which we performed careful measurements over temperature to determine the phase and group delay sensitivities per unit length. The measured values were in line with the theoretical estimate based on the coefficient of thermal expansion, with a phase sensitivity of 0.71°/°C/m.

F. System Model

The last step in performance characterization is to use all the inputs from the previous models to compute the final interferometric phase and height error. For this, we also developed various models with increasing level of fidelity, at the expense of complexity and flexibility (Fig. 14).

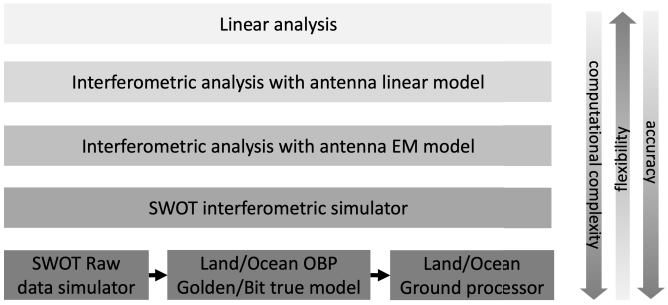

Fig. 14. System modeling tools used to assess the KaRIn performance.

1) System Linear Analysis: The system linear analysis is an excellent tool to understand the different error contributions and their sensitivities. The various error sources are evaluated separately, and then, the overall error is computed as the sum of their individual PSDs under the assumption that they are uncorrelated. The sensitivities are based on a combination of measurement, analysis, and simulation.

Fig. 15 shows our best estimate for the different systematic error sources prior to launch using S/C pointing control requirements and under the assumption that no calibration is applied. As previously explained, the systematic error is dominated by gyro roll knowledge for wavelengths longer than 25 km and the $1/f$ electronics noise for shorter wavelengths. The roll control and differential phase drifts are temperature driven and become an important error source at longer wavelengths. APR2 data [37] and experimental aircraft flights were used to bound the LDR and SDR PSDs. All other error sources are substantially smaller and mostly negligible. The total pre-launch estimate had at least 38% margin over the requirement.

2) Interferometric Analysis: In order to fully assess possible correlations between different error sources as well as to include the 3-D dispersive antenna patterns, we used the interferometric analysis tool. This tool solves for the analytical interferometric coherence derived in [24] for a spherical surface (which does not need to match the reference surface used for image co-registration). This interferometric tool has been validated using high-fidelity raw data simulations and is significantly less computationally expensive than such simulations.

The inputs to the interferometric analysis tool can be either the outputs from the antenna linear model (baseline orientation, differential phase, and group delay) or the 3-D dispersive patterns as a function of time and beta angle.

3) SWOT Interferometric Simulator: The SWOT interferometric simulator uses the azimuth and range point target responses (different for LR and HR) and convolves them with the surface in order to assess the impact of varying topography and backscattering.

This simulator is computationally expensive and so is not typically used for performance analysis. However, it was heavily used for analyzing the surf-board effect [29].

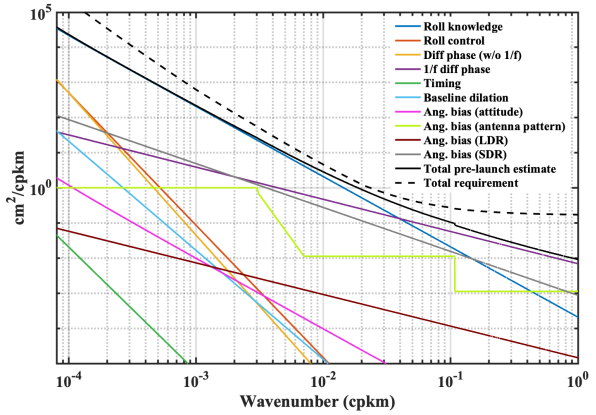

Fig. 15. Systematic error budget pre-launch estimate. The total pre-launch estimate (black solid) has a minimum 38% margin compared to the KaRIn requirement (black dashed). The dominant error source for most wavelengths is the roll knowledge from the gyro ARW (blue). The differential phase from the $1/f$ RF electronics noise (purple), if uncalibrated, can dominate the error at wavelengths shorter than 25 km. Errors due to thermoelastic roll (red) and differential phase (orange) drifts increase at longer wavelengths. The angular phase bias error due to lack of antenna knowledge (lime) is driven by the S/C control, for which here we conservatively assumed the requirement. Other error sources have a minimal performance impact. These include angular phase bias errors originating from geophysical errors such as LDR and SDR (brown and gray, respectively), angular phase bias due to attitude control (magenta), timing (green), and baseline dilation (cyan).

4) SWOT Raw Data Simulator: This is our highest fidelity simulator that creates KaRIn-like echoes as a superposition from multiple point targets within each resolution cell.

The outputs of the raw data simulator are used to perform our most detailed end-to-end and flight-like validation of KaRIn's function and performance, as illustrated in Fig. 13(c). A series of realistic simulated targets is played back by the DTS and injected into KaRIn's test ports. The scene includes realistic attitude, sigma0, and topography, and spans both ocean and land, pole crossings, and both ascending and descending passes. We assume a realistic realization of the orbit that deviates from the nominal reference orbit. This orbit is translated to S/C position commands such as those that DORIS sends to KaRIn in flight. The KaRIn 1553 command simulator sends these as well as the 1-pulse/s timing signals and the time broadcast message used for time tagging and other ground commands to KaRIn.

There are three objectives for this test.

1) Functional verification of the firmware and FSW by comparing the actual KaRIn outputs [from the solid state recorder interface (SSRI)] with the output of the firmware (BTM) and the floating-point FSW model.
2) Comparison of the BTM with the floating-point golden model to verify the BTM was implemented correctly.
3) Comparison of the BTM with the analytical tools to assess end-to-end performance.

V. KaRIn Commissioning

SWOT launched from Vandenberg Space Force Base on December 16, 2022 (see timeline in Fig. 16). The antennas were successfully deployed over four days during the Launch and Early Orbit Phase (LEOP), a process that was completed on December 22. Two cameras focused on the KaRIn antennas

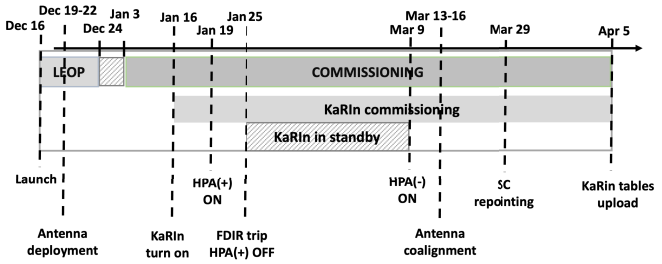

Fig. 16. KaRIn commissioning timeline.

captured the mast extending out from the S/C and locking in place but stopped short of capturing the antennas being fully deployed. Nevertheless, we confirmed deployment with telemetry data.

SWOT commissioning started on January 3, and the KaRIn turn-on procedure started on January 16. Initial checks were performed to verify the functionality of the OBP by using internal built-in test modes. The primary HPA on the plus side was finally turned on January 19. The first images that were downlinked from the LR onboard processor provided a first visual demonstration of KaRIn's striking performance. Fig. 17 is a sample of the center beam from LR data that illustrate several aspects of KaRIn's performance. Over the ocean, the interferogram phase is nearly constant due to the mild topography, and we can observe interferometric fringes even over land due to the high SNR. There is an interferometric phase offset between the two swaths that is removed during ground processing. Coherence is high with values above 0.9 over most of the swath over the ocean for low SWH, and the power shows distinct features without much speckle noise due to a large number of looks.

This particular scene was also selected to illustrate a grid-pattern artifact at the center of the image, sometimes observed at coastlines and over calm inland water bodies. This is due to the limited dynamic range in the fixed-point fast Fourier transform (FFT) used in range compression. The range compression in the LR product was optimized for the open ocean, so over land and ice and at their interface with ocean, there are occasionally bright targets that saturate the FFT and corrupt the image. This has no impact on performance since the LR product is only required to meet performance over open ocean, and coasts and land are captured with the HR product.

Unfortunately, about a week after turn on the HPA triggered an overcurrent protection circuit in the S/C and was shut down. After careful investigation by the teams, it was determined that there is no specific evidence pointing to a hardware failure on the HPA. However, it was decided to switch to and turn on the redundant HPA(-) on March 9, which has been working nominally ever since.

KaRIn commissioning consisted of the following main steps:

1) gyro calibration, attitude restitution, and verification;
2) initial point target response and time-tagging verification;
3) initial estimation of group delay;
4) estimation of antenna pointing;

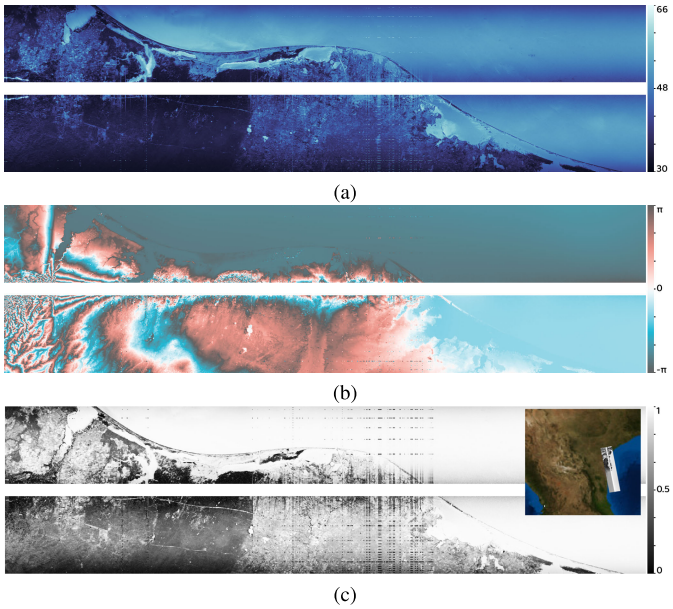

Fig. 17. Snapshot of KaRIn LR data in a descending pass going into the Gulf of Mexico as shown in the inset. The three panels correspond to power, interferometric phase, and coherence for both swaths. The vertical axis corresponds to the cross-track direction (5–65 km for each swath) and the horizontal axis spans 500 km in the along-track direction. The small gap between the swaths corresponds to the ±5-km gap that will be filled by the NA data. (a) Power (dB). (b) Interferometric phase (rad). (c) Coherence.

5) antenna co-alignment to minimize differential pointing;
6) S/C repointing;
7) final estimation of group delay and differential group delay;
8) verification and optimization of onboard tables and OBP.

In the following sections, we describe the most important aspects of these steps.

A. Attitude Restitution Verification

As discussed in Section III-E, the rigid-body roll knowledge is the largest contribution to KaRIn's systematic error budget, so it was critical to validate the ground attitude reconstruction.

The SWOT project decided to invest in two attitude reconstruction tools: the operational one, which was developed by our CNES partners, and a test bench, which was independently developed by JPL. The two teams worked closely in cross-verification efforts using simulated data prior to launch.

It is not straightforward to perform the cross verification in flight since we do not have truth data as in simulations. In addition to that, even though this is a dominant error source, it is still well below the ocean topography signal, so the error is hard to separate from the ocean signal in the absence of ground truth, which we did not have during commissioning. The approach we took is as follows.

1) The difference between the two attitude restitutions was verified to be below the gyro's ARW at the frequency range of interest and the bias between them to be within measurement error.
2) At certain beta angles, SWOT performs a solar array rotation. We knew, per pre-launch simulations, that this would create a strong roll signal. In flight, we confirmed that this roll signature appears as distinct peaks above the ocean signal, which were able to verify that the attitude reconstruction was able to suppress that signature by at least four orders of magnitude.

Fig. 18 illustrates an example of the verification performed during a solar array rotation. The blue curve corresponds to the PSD of the measured data during this period prior to correcting the S/C roll. The peaks observed at wavenumbers about 1/25, 1/12, and 1/2 km are not real ocean signatures but originate from S/C roll errors. When applying the roll correction from the attitude reconstruction (red), these peaks are significantly reduced. However, we observed that if the gyro's time tag is shifted by 1/2 gyro sampling period, those peaks are consistently better suppressed for both JPL and CNES reconstruction tools. It was not possible to verify the time-tagging accuracy by test prior to launch. Even though we could not find the root cause for this apparent time tag error, we recommended implementing this shift operationally given the empirical evidence.

One can observe in the figure an 8-Hz spurious signal (equivalently, 1-/0.8-km wavenumber), which is not suppressed by the gyro and is quite strong during solar array rotations. We believe that it is due to an expected dynamic disturbance in the mast or reflectarrays that is not captured by the gyro measurement. As designed, this frequency is above 7 Hz (see Section II-C2).

Fig. 19 shows a typical PSD for the roll attitude reconstruction (i.e., our best knowledge of the S/C roll) when converted to height error (gray). There are some S/C modes that create spectral peaks over the gyro's ARW (dashed). Assuming that we also achieve the four-order magnitude reduction during nominal operations, this is sufficient to suppress that the roll error during nominal science data captures to below the requirement (black solid) and even to below the measured noise floor (solid dotted). Note that the peak at a wavenumber of about 1/2 km is caused by a known gyro effect and so will not be suppressed, but it is well below the measured noise floor.

B. Point Target Response, Time Tagging, and Group Delay Estimation

The SWOT project deployed several corner reflectors to be used during commissioning and the calibration and validation phases at different cross-track locations at the Oklahoma crossover. Fig. 20 shows a typical point target response over a corner reflector at about 33-km cross track using data collected with the raw data mode. It was processed with the SWOT SLC processor (developed by the algorithms team) with a 0.1-s azimuth integration time and no apodization. This resulted in the expected 3.8-m azimuth resolution and 1.8-m range resolution. Using this type of data, we were able to confirm the purity of the point target response and the accuracy of the time tagging (from azimuthal shifts) and estimate the group delay for each channel (from range shifts).

The time-tagging error was determined to be less than 0.2 m (about 30 μs).

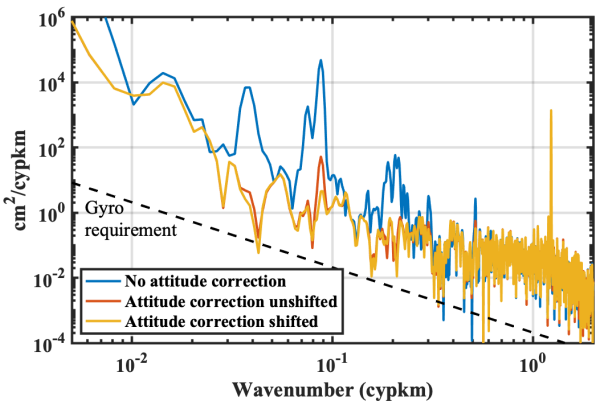

Fig. 18. Ocean height PSD at a typical solar array rotation before correcting for roll (blue). The solar array rotation excites S/C modes that appear as peaks in the PSD. After applying the attitude reconstruction, those peaks are significantly reduced (red). When a 1/2 gyro sampling interval correction is applied to the gyro's time tag, the spurious signals are suppressed even further by at least four orders of magnitude (yellow). The large spur at 1/0.8-km wavenumber is due to an expected dynamic disturbance that is not captured by the gyro measurement.

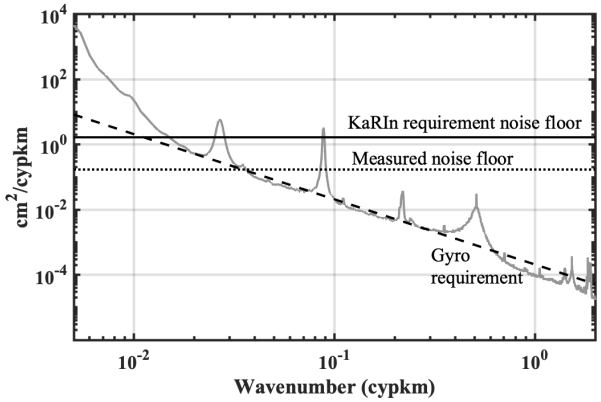

Fig. 19. PSD for nominal S/C attitude obtained from the attitude reconstruction and converted to equivalent height error (gray). One can observe S/C modes above the gyro's AWR noise (dashed). Assuming that these are suppressed by four orders of magnitude, these would get reduced well below the KaRIn requirement noise floor (black solid) and the measured noise floor (dotted). The peak at 0.5 cpkm is a known gyro error, so it will not be suppressed.

C. Differential Group Delay Estimation

The differential group delay (defined as the difference in group delay between the two interferometric channels) per polarization was estimated from the SWOT HR SLC data over several sites spread over various latitudes, longitudes, and terrain types. Differential group delay was estimated by maximizing interferometric correlation magnitude as a function of a scalar differential delay as the two images are interpolated to the same geometry. The scalar delay that maximizes coherence corresponds directly to the differential delay, given as

$$\hat{\tau}_d = \max_{\tau} \left\{ \left| \frac{\left\langle s_1^i(t+\tau) s_2^{i*}(t) \right\rangle}{\sqrt{\left\langle s_1^i(t+\tau) s_1^{i*}(t) \right\rangle \left\langle s_2^i(t) s_2^{i*}(t) \right\rangle}} \right| \right\} \tag{13}$$

where s_1 and s_2 are the two interferometric SLC images. The differential delay was estimated continuously during KaRIn commissioning, with an estimated mean differential group delay of -31.05 ps for H-pol and -65.11 ps for V-pol

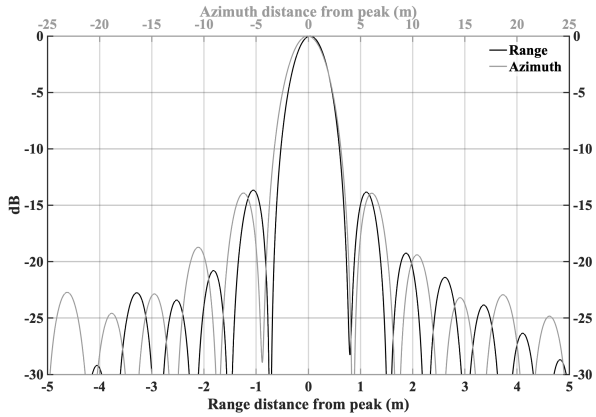

Fig. 20. Point target response over corner reflector in range (black) and azimuth (gray). No apodization was applied during processing, resulting in approximately a 14-dB sidelobe ratio. The resolution is 3.8 m in azimuth with 0.1-s azimuth integration time and 1.8 m in range.

and a standard deviation of approximately 3.5 ps for both polarizations. This small differential group delay introduces negligible decorrelation (less than 0.9998).

D. Antenna Co-Alignment and S/C Repointing

The differential azimuth pointing is a critical KaRIn requirement. Since it was expected that the requirement would not be met right after launch, the mechanical team developed alignment mechanisms to rotate each antenna independently. This provides a sufficient level of freedom to compensate for both a differential pitch and a differential yaw. The mean pitch and yaw can be removed by repointing the S/C.

In addition, we developed a robust tool to estimate each antenna's pointing. The antenna attitude estimation tool consists of two parts: a gross estimation of the Doppler ambiguity and a fine estimation of attitude from the Doppler measured over the ocean.

Different algorithms were used for ambiguity estimation, including standard ones such as multilooked cross correlation [38] and the SNR loss incurred when compressing a corner reflector with the wrong ambiguity, and KaRIn-specific ones, such as the magnitude and shape of the systematic phase bias. After receiving the first KaRIn data, it was immediately clear that the antennas were not on an ambiguity; SNR was high and similar for both channels, and the point target response over the corner reflector and the phase bias were as expected.

The OBP computes the Doppler phase via a pulse-pair algorithm, and this phase was used for fine attitude estimation. We created a forward model to estimate Doppler from the antenna pattern weighted average of the instantaneous along-track frequency of the target return. A minimizer can then be used to find the transmit and receive antenna attitude that produces the best match for the Doppler phase. Since running this minimizer continuously is computationally expensive, we tabularized the results as a function of various parameters, to be used as an inverse model for efficiently determining the attitude.

The differential pitch bias after launch was determined to be about 25 mdeg, which was within the expected range of values

but did not meet the requirement. It was therefore decided to operate the alignment mechanisms to minimize the differential pointing.

Based on simulated data, we knew that the differential pitch variation over beta angles was expected to be less than 8 mdeg (from Fig. 12(a), which is a bounding simulation with some conservative assumptions). In addition to that, the alignment mechanism also deforms with temperature, causing a differential pitch variation of approximately 6 mdeg. The original plan was to measure the variation of differential pitch over beta and perform the alignment afterward, to minimize the average differential pitch over beta. However, we were not able to collect that data due to the HPA anomaly, so the co-alignment was done based on data for a small range of beta angles.

We used our best judgment from simulated data and set a goal of -4 mdeg at the beta angle at which coalignment was performed. To minimize operational risks, we only moved one of the alignment mechanisms since the resulting differential yaw was expected to be small and within the requirements. We achieved our goal with an uncertainty of less than 1 mdeg.

We also estimated antenna pointing in elevation using the expected signal power as a function of elevation. The accuracy of this approach is at best about 20 mdeg, but this is sufficient for performance. The measured mispointing in elevation was around 20 mdeg for the transmit antenna and -50 mdeg for the receive antenna, with similar values for H and V swaths.

The last step was repointing the antennas for close to zero mean attitude bias. This was achieved by commanding the S/C AOCS to follow a frame that was rotated from the original target frame by less than 20 mdeg, which was consistent with our pre-launch simulations.

E. Onboard Table Verification

The FSW floating-point model was used to verify that the interaction between FSW and firmware was working as expected and that the onboard tables were not only being followed as planned but also that the content was correct. This model checks the self-consistency of all the firmware fields, so it is able to verify that the packets are being formed correctly.

The estimated group delay parameters and flight loopback data were then used to refine the static parameter table and the range compression reference functions.

We also optimized the Doppler computation averaging window. The OBP has the option to estimate a cross-track linear fit to Doppler over the ocean, but it was determined that performance was best using a fit that is constant in cross track.

The last step before moving to the calibration phase was uploading the updated tables and verifying that they were working correctly.

VI. KaRIn In-Flight Performance and Comparison to Pre-Launch Measurements

In this section, we will look into how the flight data compare to our pre-launch expectations and also provide explanations for the major discrepancies.

Note that this analysis is done using only KaRIn data, without any other instrument or ground truth (which is the focus of the SWOT validation campaign, rather than commissioning). As such, we do not attempt to validate SWOT's error budget, but we provide evidence that the instrument is working as expected.

A. Random Performance

To assess the random performance against the pre-launch estimate, we used the LR product, as this can be used without any further processing.

In order to perform the comparison, data over rain-free ocean with SWH about 2 m were used (note that the requirement was constructed assuming a 1-dB atmospheric attenuation due to rain). We determined which areas are rain-free using the Integrated Multisatellite Retrievals product of GPM constellation (IMERG) database [39], and for SWH, we used the European Centre for Medium-Range Weather Forecasts (ECMWF) model [40] (the KaRIn data product includes this SWH value interpolated in the swath [41]). KaRIn was launched with a healthy 4-dB margin for end-of-life (EOL) conditions thanks to the KaRIn electronics and antenna meeting or outperforming their requirements. There was about a 2-dB additional margin allocated to antenna gain, decorrelation, and noise figure measurement uncertainty. The SNR degradation that will be experienced over the life of the mission due to reduced transmit power and radiator degradation was estimated to be at most 1.6 dB. Therefore, at launch, we expected to have approximately 8.6 dB of SNR margin relative to the requirement over rain-free ocean.

We used a statistical approach to assess the received signal power. We binned the data as a function of ECMWF model wind speed and then computed the difference between the received signal power and the expected signal power when using the Vandemark-2004 sigma0 model [23] given the ground-measured antenna and RF gains. The resulting difference is 1–1.5 dB at the requirement's 8.9-m/s wind speed. In practice, there are uncertainties in the gain budget, for example, in the antenna gain and transmit power, and producing a wind speed model function from sigma0 is part of the validation campaign. For our purposes of assessing SNR, since the Vandemark model was used to construct the error budget, this results in about 1.3-dB additional margin, bringing the overall SNR margin to close to 10 dB at launch over rain-free ocean.

Fig. 21 shows the SNR and coherence measured with the LR product during the science orbit at an altitude of about 896 km over an area of rain-free ocean that had a fairly stable wind speed of 8.9 m/s and an SWH of 2 m. One can observe that the $\pm N$ beams have about the same SNR and coherence, which indicates that the Doppler centroid is being computed correctly and that the antenna pattern is fairly symmetric. Fig. 22 shows the different decorrelation terms explained in Section III-F for this scene as a function of ground range. One can observe that thermal decorrelation is the dominant random error source at these SWH and wind speed conditions. In this example, the geometric decorrelation calculation assumes an ideal transmit and receive spectral response, and the electronics decorrelation

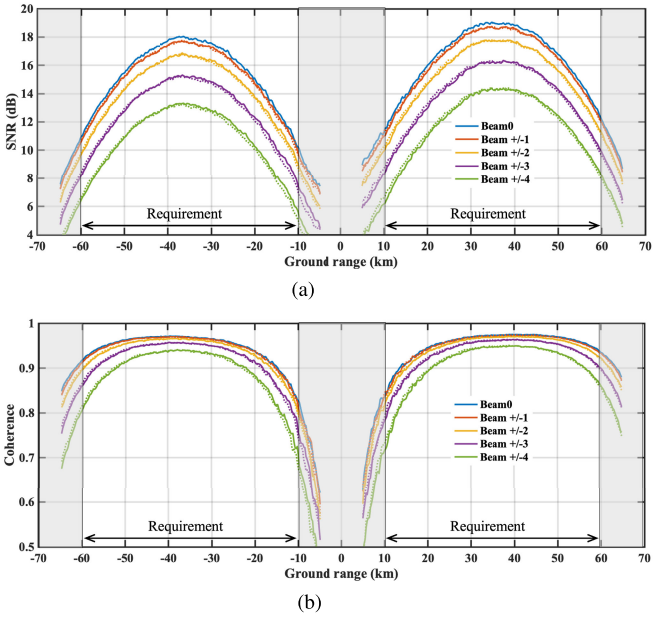

Fig. 21. Measured SNR and coherence for the science orbit over rain-free ocean for 8.9-m/s wind speed and 2-m SWH. The beams are labeled from -4 to $+4$ with 0 the center beam (most closely aligned with the antenna boresight). Solid line is for $+N$ beams and dashed line is for $-N$ beams. (a) SNR. (b) Coherence.

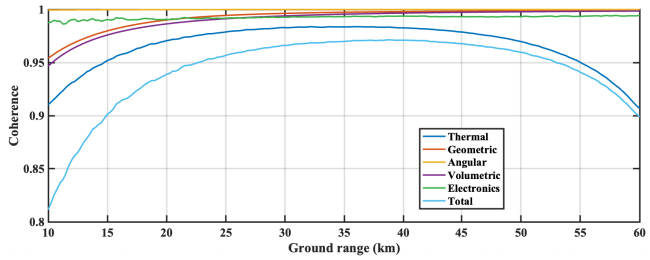

Fig. 22. Coherence as a function of cross track for 8.9-m/s wind speed and 2-m SWH for the center beam (beam 0). Thermal decorrelation is the dominant random error source at these SWH and wind speed conditions, together with geometric and volumetric (due to SWH) decorrelations, which increase in the near range.

includes the impact of that as well as the image and LO leakage.

The height error can be estimated from the coherence and is illustrated in Fig. 23 as a function of ground range for both the measured flight data and the pre-launch estimate (with 4 dB of SNR margin), which assumes EOL conditions and 1-dB rain attenuation. The height error (RMS over the swath) was estimated to be 1.8 cm for 1-km pixels using the pre-launch estimate, whereas the measured error over rain-free ocean is 0.8 cm.

B. SWH and Volumetric Correlation

The SWOT requirements were derived for SWH of 2 m, which is approximately the global average. However, there are areas of large SWH that are of great interest to oceanographers, so it is important to characterize KaRIn's performance over SWH. A thorough calibration and validation of the volumetric correlation for the purposes of estimating SWH is part of the calibration and validation campaign, but in this section, we assess KaRIn's requirement compliance.

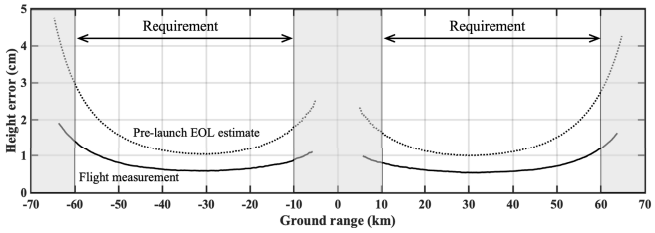

Fig. 23. Estimated random height error for 1-km pixels from coherence for 8.9-m/s wind speed and 2-m SWH. The flight measurement (solid) uses rain-free data. The pre-launch estimate (dotted) assumes EOL conditions and 1-dB rain attenuation. Under these conditions, the height error (RMS over the swath) was estimated to be 1.8-cm pre-launch, whereas the measured error is 0.8 cm.

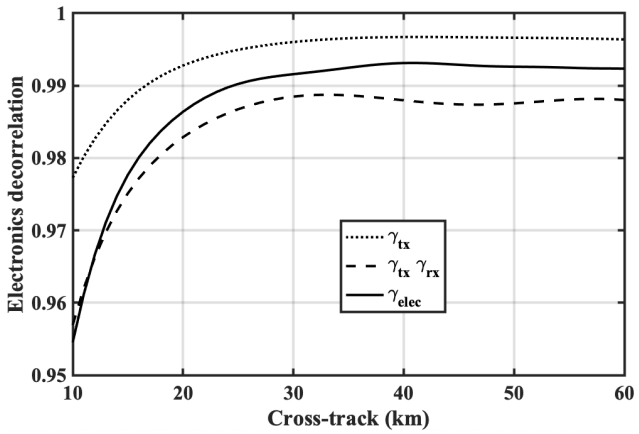

Fig. 24. Electronics decorrelation. Dotted line is the pre-launch estimate for the decorrelation due to the transmit pulse, dashed line is the pre-launch estimate for the total electronics decorrelation, and solid line is the electronics decorrelation estimated in flight. As expected, the pre-launch estimate for total decorrelation was conservative since it included the impact of test equipment.

The first step to verify the volumetric decorrelation is to estimate the electronic contribution to the decorrelation. We used two days of rain-free ocean data during the one-day orbit with 2-m SWH and wind variation over the swath less than 0.2 m/s. By comparing the measured correlation to the theoretical correlation, we derived a $+0.15$-dB correction to the SNR and the electronics decorrelation term. The small SNR correction is attributed to the uncertainty in the receive noise measurement due to LO leakage and the receiver frequency response. The flight estimate of the electronics decorrelation, γ_{elec}, shown in Fig. 24, falls as expected between the decorrelation due to the transmit pulse shape, γ_{tx}, and the total decorrelation measured during ground tests, $\gamma_{\text{tx}}\gamma_{\text{rx}}$, which was impacted by the test equipment as explained in Section IV-E.

Using the estimated electronics decorrelation and rain-free ocean, we assessed the volumetric correlation as a function of SWH and cross-track distance. Fig. 25 shows that the volumetric decorrelation term is well estimated by the theoretical expression. Given the significant SNR margin, the total coherence at 10 km remains higher than 0.5 even for SWH near 6 m (assuming 8.9-m/s wind speed).

C. Surf-Board and Backscattering Modulation

An important error source as the SWH increases is the so-called "surf-board" sampling and backscattering modulation, as explained in [29]. In that paper, we showed

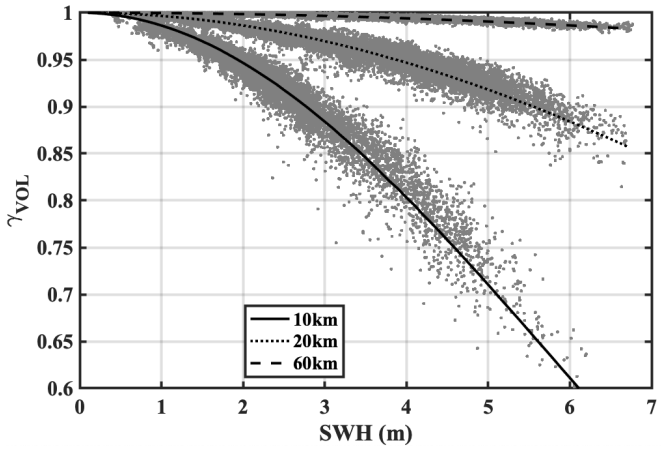

Fig. 25. Volumetric decorrelation as a function of SWH. The gray dots are the measured values, and the solid (10 km), dotted (20 km), and dashed (60 km) curves correspond to the theoretical expression at the specified cross-track distances.

that the impact of these nonlinear mechanisms on KaRIn performance depends significantly on the wave spectrum characteristics such as direction and energy wavelength centroid. We also introduced an approximate model for the height error variance due to the surface waves not including volumetric decorrelation, $\sigma_{h_{\mathrm{SWH-NL}}}$, as a function of cross track, C, that we used for the purpose of incorporating this error in KaRIn's overall error budget

$$\sigma^2_{h_{\mathrm{SWH-NL}}} = C_{\sigma_0} + \frac{C_{\mathrm{SB}}}{C^2}. \tag{14}$$

There is a constant term, C_{σ_0}, which is to first order related to the backscattering modulation, and a term proportional to C_{SB} and varying inversely with ground range squared, which is to first order attributed to the surfboard sampling.

Simulations also indicated that the error power spectrum resembles that of white noise. However, it is not strictly a random error since, theoretically, it could be removed if the wave spectrum were known exactly. This is in practice impossible, so we treated it as a random error in the error budget.

We verified the accuracy of our pre-launch simulations using four cycles of flight data collected during the science orbit using the following methodology. The SSHA PSD was first computed for the 500-m resolution 250-m posting product as a function of cross track for 500-km-long patches of rain-free ocean with fairly uniform wind speed and SWH (from ECMWF). We excluded from this analysis areas with strong swell that manifests themselves with distinct structures in the along-track spectrum. The height error PSD due to decorrelation was then estimated as a function of cross track using the measured decorrelation and the estimated number of looks. Fig. 26 illustrates this procedure for a case with SWH 5 m. The top panel shows the SSHA PSD averaged from 10 to 60 km in cross track (blue), the error estimated from decorrelation (red), and the difference between them (yellow). The integrated signal between frequencies 0.2 and 0.4 cy/km is used to estimate the height error. Fig. 26(b) shows the height error as a function of cross track. The total height error is

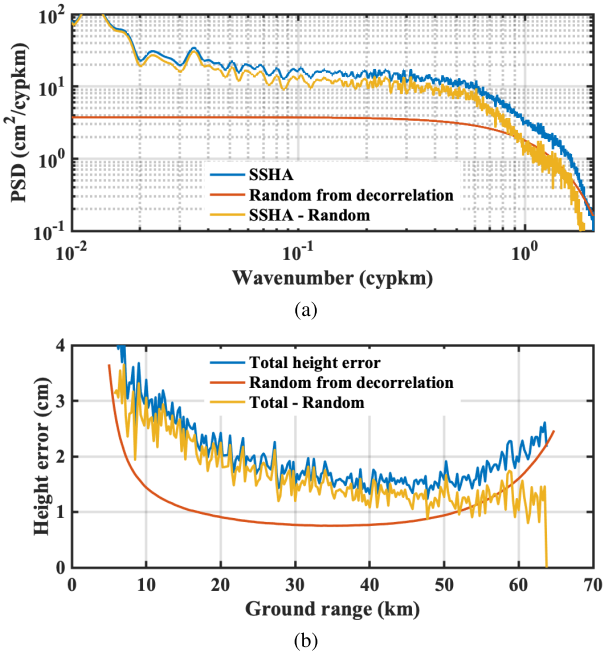

Fig. 26. Example of separating nonlinear wave effects from random error due to decorrelation for a case with SWH 5 m. PSD and height error are shown for the measured SSHA (blue), estimated from decorrelation (red), and difference between them (yellow), which is associated with nonlinear wave effects. (a) PSD averaged over swath. (b) Height error as a function of cross track.

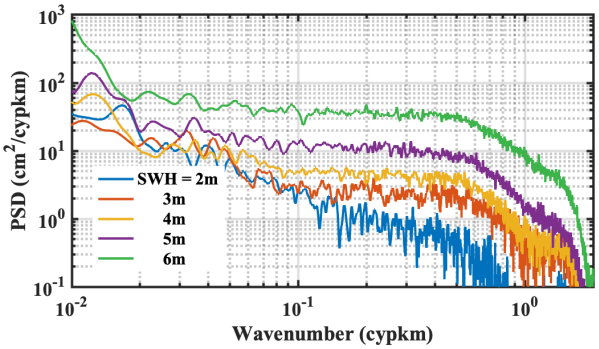

Fig. 27. Height error PSD due to nonlinear wave effects for different values of SWH computed using the 500-m resolution product.

shown in blue, and after removing the random error obtained from the decorrelation (red), we obtain the error attributed to nonlinear wave effects in yellow. This error approximately follows the expression in (14).

Based on our simulations, we believe that this method provides an approximate value for the impact of waves on performance. However, as SWH is reduced, the magnitude of the nonlinear error can drop below the actual topography signal, and since it is not possible to separate them, the estimate is less accurate. Fig. 27 shows the PSD of the SSHA minus the decorrelation part for different values of SWH. For high SWH, the spectrum is flat over the region from 0.2 to 0.4 cy/km and appears to be dominated by the nonlinear wave effect. However, for SWH 2 m, the PSD could well be mostly coming from the ocean topography itself.

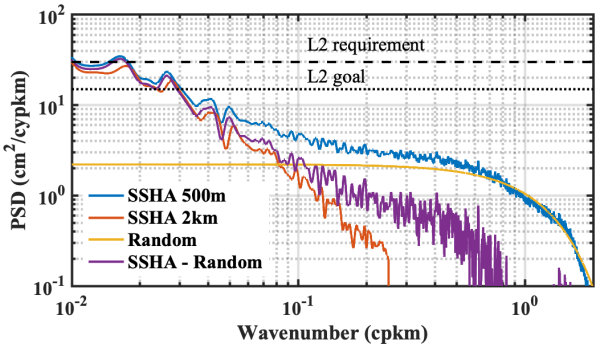

(a)

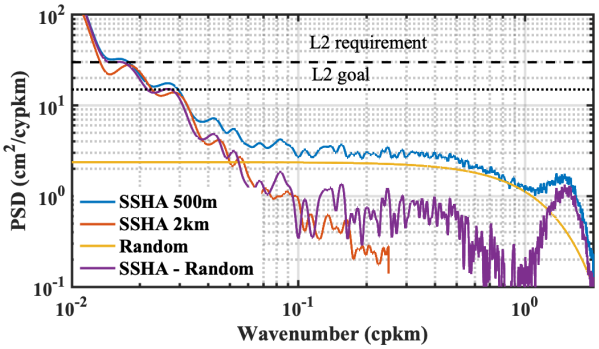

(b)

Fig. 28. Two additional examples of height error PSD for SWH 2 m and wind speed around 8.9 m/s. The curves correspond to the SSHA PSD averaged over the swath for the 500-m resolution product (blue), the SSHA PSD for the L2_LR_SSH 2-km resolution product described in [41] (red), the random error PSD from decorrelation for the 500-m product (yellow), and the difference between the SSHA PSD and the random error PSD for the 500-m product (purple). (a) We show the L2 requirement of 2-cm^2/cpkm (dashed) and the 1-cm^2/cpkm goal (dotted) scaled by a factor 7.5/0.5 to account for the fact that the L2 requirement is specified for cross-track pixels of 7.5-km resolution, to compare to the PSDs using the 500-m resolution product. The random noise component is below the requirement by about one order of magnitude. (b) We can observe a spectral peak at wavenumber greater than 1 cpkm, corresponding to the along-track waves (likely due to swell), even though these are largely attenuated by the OBP averaging window.

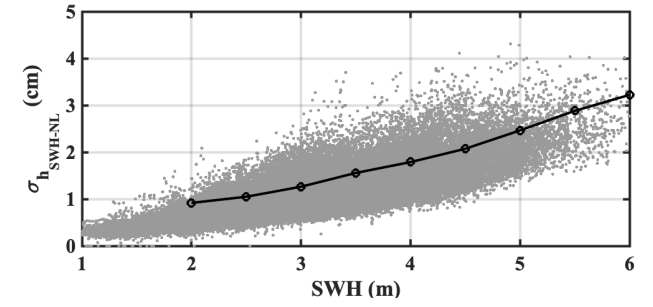

(a)

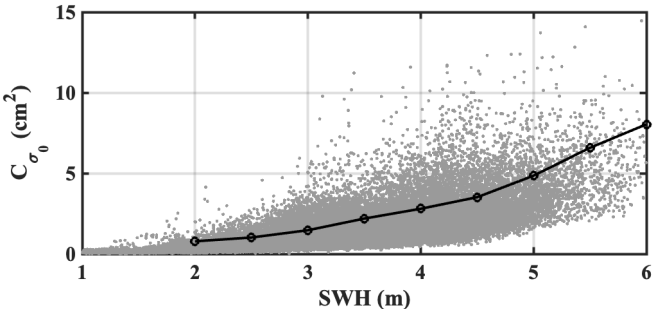

(b)

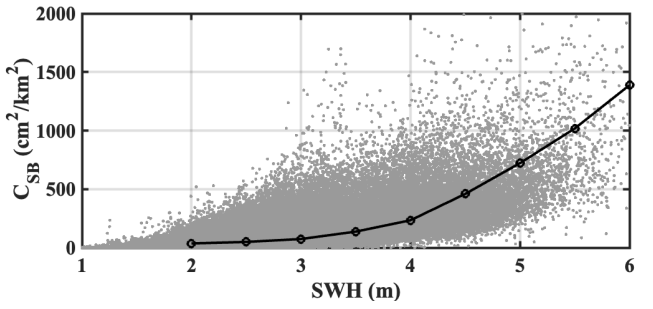

(c)

Fig. 29. Height error due to nonlinear wave effects and approximate model coefficients per (14). The gray points correspond to the measured data and the black line corresponds to the pre-launch estimate from the simulated data. (a) Height error due to nonlinear wave effects (RMS over the 10–60-km swath). (b) Backscattering modulation coefficient. (c) Surf-board sampling coefficient.

Fig. 28 shows two different cases with an average SWH of 2 m and a wind speed of 8.9 m/s. The first observation is that the white noise level of the KaRIn measurement (blue), as well as the random error (yellow), is about one order of magnitude below the requirement (in units of wavenumber spectra cm^2/cpkm, not in units of height error), which is consistent with our previous results on flight SNR. The difference of the 500-m SSHA PSD and the random PSD at this SWH (purple curve) can still contain nonnegligible ocean topography. For some cases, such as in (b), a spectral peak corresponding to along-track waves can be observed. The signature of these along-track waves is highly attenuated by the along-track averaging window in the LR OBP.

Using this type of analysis, we computed the RMS height error from 10 to 60 km in cross track as a function of SWH. We also fit the height error dependence versus cross track to the model in (14) to empirically obtain the two coefficients. Fig. 29 shows the total error (a), backscattering modulation coefficient (b), and surf-board sampling coefficient (c), as a function of SWH. The black curve is the model derived from simulated data and presented in [29], which was computed from the average height error variance at each SWH using a large sample of wave spectra. One can see that the surf-board and backscattering modulation coefficients match the simulated predictions fairly well (the value assumed for the hydrodynamic modulation might have been slightly pessimistic, but a more detailed analysis will be needed to determine that).

Finally, Fig. 30 shows the overall height error as a function of ground range for different values of SWH for 1-km^2 pixels. The top figure shows the total RMS error across the 10–60-km swath, which goes from 1 cm for SWH of 2 m to 3 cm for SWH of 6 m. Due to the excellent random thermal performance, the KaRIn random requirement (Section III-B) is met even for SWH close to 6 m. The bottom figure shows the contribution due to only decorrelation sources.

D. Pointing Performance

Fig. 31 illustrates the mean and differential pitch and differential yaw measured using the method described in Section V-A as a function of beta angle, after averaging to

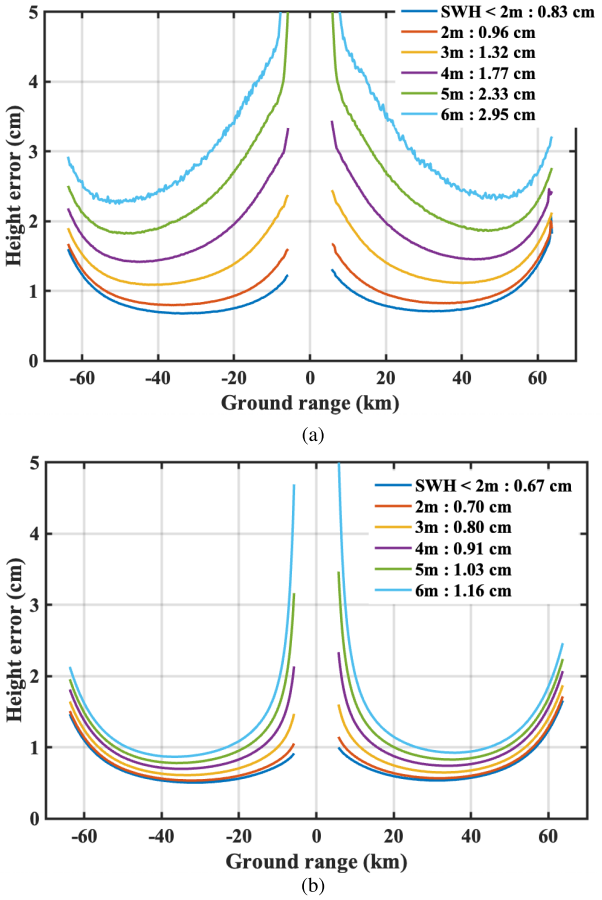

Fig. 30. Height error as a function of ground range for 1 km^2 pixels. Blue is for SWH less than 2 m, and the other curves are for the indicated value ±0.5 m. The RMS error from 10 to 60 km is indicated for each SWH range. Due to the excellent random thermal performance, the KaRIn random requirement is met even for SWH close to 6 m. (a) Total height error. (b) Height error due to decorrelation.

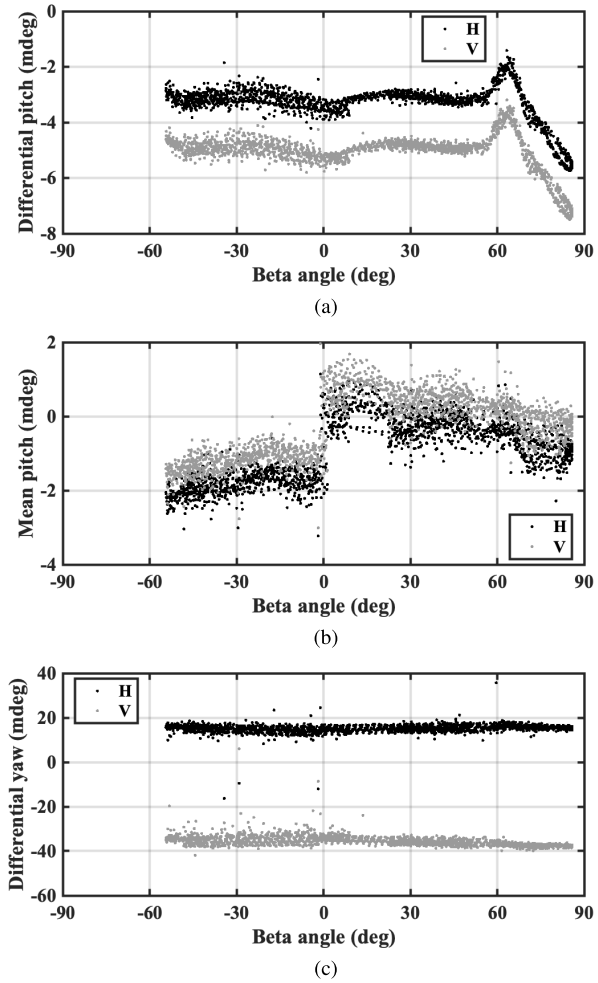

Fig. 31. Pointing performance as a function of beta angle for H (black) and V (gray) polarizations. (a) Differential pitch. (b) Mean pitch. (c) Differential yaw.

remove S/C control attitude errors in pitch. The differential pitch sensitivity with beta angle is excellent, with only 4 mdeg of change over beta. This is less than our simulations predicted, which is not totally unexpected given that the simulations assumed bounding conditions. The differential pitch and yaw exhibit repeatable behavior as a function of the absolute value of beta angle. For mean pitch, there is a small 2-mdeg jump at yaw flips that is attributed to a small bias change in the star tracker measurement because of the different viewing geometry. The precision of the mean yaw measurement is not sufficient to observe any appreciable dependence with beta angle due to the error introduced by an apparent cross-track surface velocity (see Section VI-E). The measured mean yaw is only about −6 mdeg for V and −13 mdeg for H swaths.

By removing the S/C attitude, we can assess the KaRIn contribution to pointing. KaRIn's pointing varies smoothly over the orbit, as predicted in simulations [see Fig. 12(a)], with about 1 mdeg of pointing drift for both mean and differential pitch.

E. Surface Velocity

Our pointing analysis revealed a linear dependence of the Doppler frequency with cross-track distance, which appears as a yaw in the attitude estimate. We believe that this apparent yaw is due to a cross-track velocity, similar to the effect described in [42], and whose magnitude cannot be explained by ocean currents. The explanation by Chapron et al. [42] is that this residual velocity is due to the waves, not the current. We have analyzed five cycles (about 100 days) of data captured during the science orbit and computed the equivalent cross-track velocity, U_D. We defined positive as the direction away from the satellite during the ascending tracks, looking to the east–southeast, and reversed the sign of the velocities measured for the descending tracks (this creates a small inconsistency in the direction since the cross-track directions are not fully aligned for ascending and descending passes, especially at higher latitudes). We used ECMWF [40] atmospheric model wind vector data at 10 m, U_{10}, to compute the wind speed in the cross-track direction, $U_{10||}$. Fig. 32 shows the heat map of the cross-track velocity, U_D, as a function of $U_{10||}$, with the color indicating percentage of occurrences in each 0.1-m/s grid point. This plot agrees well with the observations in [42], even though this is at a different frequency and viewing geometry. We also observe the saturation of U_D at the highest wind speed, but U_D is a larger percentage of $U_{10||}$, at about 50%

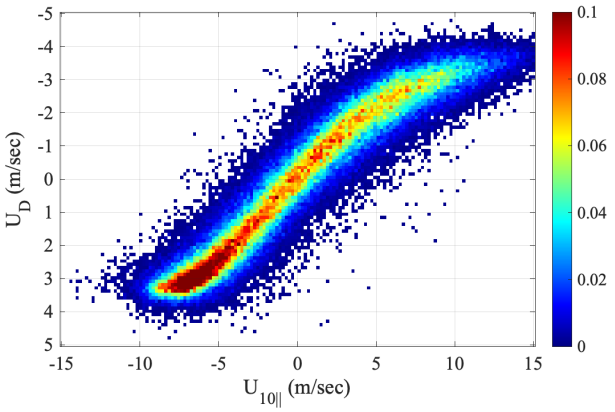

Fig. 32. Joint distribution of observed cross-track surface velocity, U_D (positive for direction away from the satellite during the ascending tracks and thus looking to the east–southeast), and cross-track wind speed, $U_{10||}$. The color indicates the percentage of occurrences in a 0.1-m/s square grid.

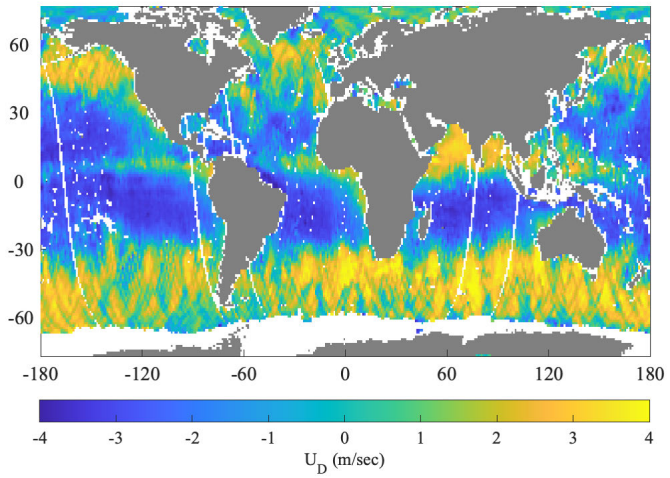

Fig. 33. Map of cross-track surface velocity, U_D, in m/s obtained from Doppler for one cycle of data collected during the science orbit, averaging over 1° square pixels the velocities in ascending passes with the negative of velocities in descending passes. The measured U_D agrees well with known atmospheric wind patterns, with prevailing winds that blow from the west at mid-latitudes (positive U_D) and trade winds that flow east-to-west in the Earth's equatorial region (negative U_D).

(compared to 30% in [42]). Fig. 33 shows the geographic map of U_D for one cycle during the science orbit, which one can observe that it is well correlated with atmospheric wind patterns.

An uncorrected cross-track surface velocity causes an apparent shift of the target location in the SAR image, which results in a retrieval height error approximated by

$$\delta h_{U_D} = C \frac{U_D}{v_p} \alpha_p \left(1 + \frac{H}{R_E}\right) \tag{15}$$

where v_p is the platform velocity and α_p is the pitch.

This error is part of SWOT's motion error budget (Section II-C5). This error was modeled using the surface velocity PSD derived from ECCO2 model data [43] and the control pitch pointing requirement of 33 mdeg. The measured apparent velocity is about one order of magnitude higher than ocean currents, which could impact the performance. However, given that the pitch control is about one order of magnitude better than the requirement, the error remains negligible.

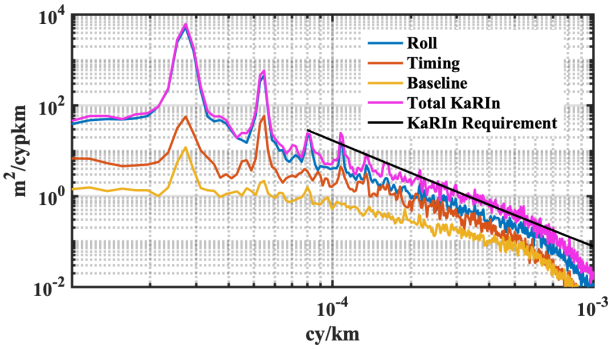

Fig. 34. PSD of systematic error components: roll (linear in cross track), timing (constant in cross track) and baseline (quadratic in cross track), and total KaRIn error (sum of all three components) compared to KaRIn requirement.

F. Thermoelastic Performance

We have evaluated KaRIn's thermoelastic performance using two methods. Assuming that the SSHA and any residual error sources, such as media or wave errors, are mean zero, we can extract the systematic error introduced by KaRIn by averaging the measured SSHA over long stretches of ocean and computing the residual. Alternatively, we can evaluate the SSHA difference at the crossover diamonds assuming that the ocean topography does not change significantly over the time between ascending and descending passes of the crossovers. Both methods provide similar results, and in this article, we will show results from using the first method since, for the one-day orbit, the spatial sampling that we get from crossovers is limited. In order to reduce some of the variability introduced by the ocean topography, we first subtract the Global Ocean Gridded L4 Sea Surface Heights [44], per recommendation of our CNES colleague Gerald Dibarboure.

We use 1000-km patches of ocean data and fit a quadratic polynomial in cross-track to the SSHA, separate for each polarization. The residual after removing this quadratic fit and a constant phase screen, and after averaging to reduce the effect of the ocean topography, is less than 0.5 mm of height error. This demonstrates the high stability of the KaRIn antenna and mechanical system.

Fig. 34 shows the PSD for the different error components (average for H and V since they are similar) computed over the complete three-month calibration phase in the one-day orbit, and the overall error PSD (adding the three error components) compared to the KaRIn requirement. Given the filtering and sampling, the result is only valid for wavenumbers longer than 0.005 cy/km. We believe that there is still residual ocean topography in these error PSDs since, for example, we were expecting the timing component to be well below the linear roll component (see Fig. 15). Still, the total error is below the KaRIn requirement and we expect it to be sufficient to meet the hydrology crossover performance. The peaks correspond to harmonics of the orbital frequency and are largely due to attitude roll reconstruction error.

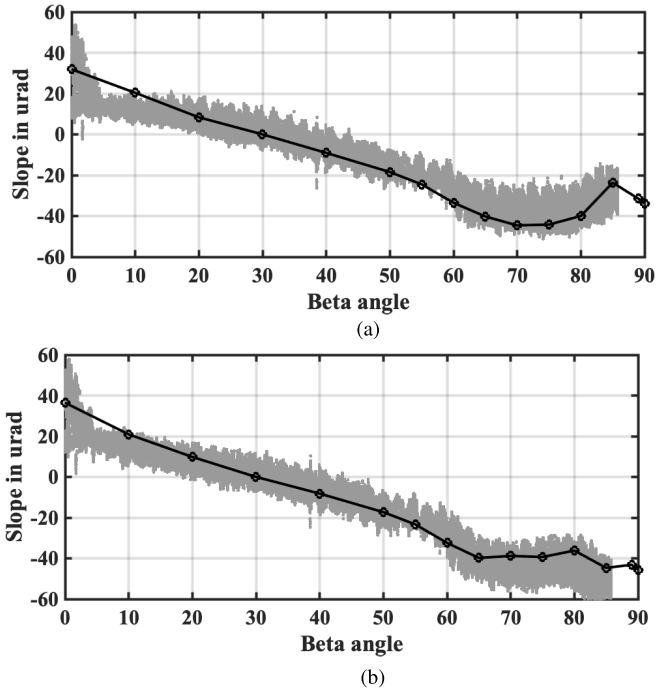

Fig. 35. Measured slope for (a) H and (b) V swaths as a function of beta angle in gray points, compared to the pre-launch estimate in black.

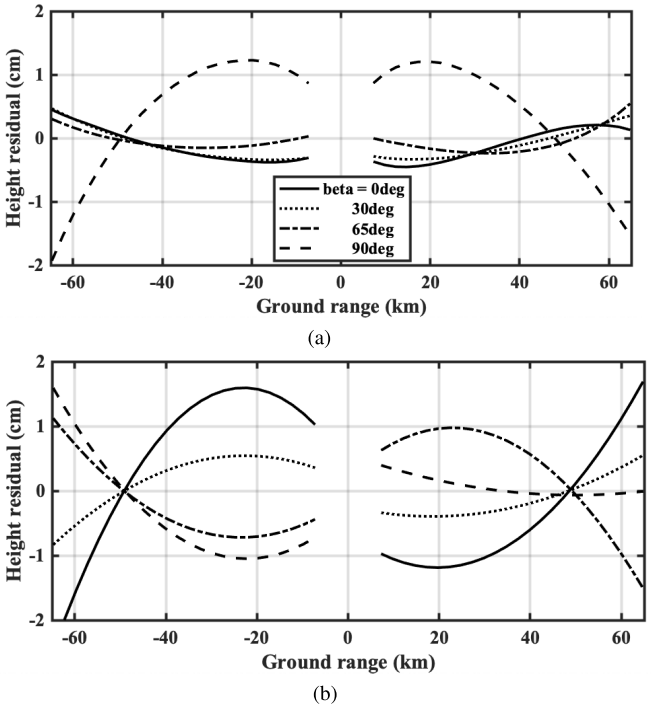

Fig. 36. (a) Simulated and (b) measured height residual after removing cross-track slope as a function of cross track for different beta angles.

The largest component in the KaRIn error is a slope in cross track originating from roll and phase thermoelastic distortions. Fig. 35 shows the measured slope as a function of beta angle compared to simulations using the linear antenna model (Section IV-C1). There is very good agreement for both H and V swaths. Note that the measurement also includes the impact of the star tracker thermoelastic distortion, which was not part of the KaRIn error budget and is not included in this simulated data. The spread in the data for a particular beta angle is due to orbital variations and is largely coming from the star trackers roll knowledge error. This behavior is clearly evident near beta 0, where the star trackers go in and out of eclipse, and the thermoelastic distortion of the star tracker brackets was expected to cause this increased error. The approximately 100-μrad slope range over beta angle creates 6-m height errors at the far range that will need to be removed with crossovers.

In order to compare our pre-launch simulations to the residual height after removing the linear part, we need to use the full EM antenna RF model (Section IV-C2). Fig. 36 illustrates that the residual is small (on the order of 2 cm), both based on pre-launch simulations and measurements. However, while the simulations predict a fairly symmetric behavior for H and V swaths, the measurement indicates an asymmetric quadratic term, which cannot be explained with a mechanical baseline dilation. Fig. 37 shows the quadratic and constant errors for H and V swaths as a function of beta angle. These coefficients diverge with opposite signs as a function of beta and are approximately correlated with the feed temperatures on the minus side, which is the one facing the Sun. Even though this behavior was not predicted by our simulations, the sensitivities derived using the linear antenna model (Section IV-C1) indicate that this asymmetry could be due to feed translations

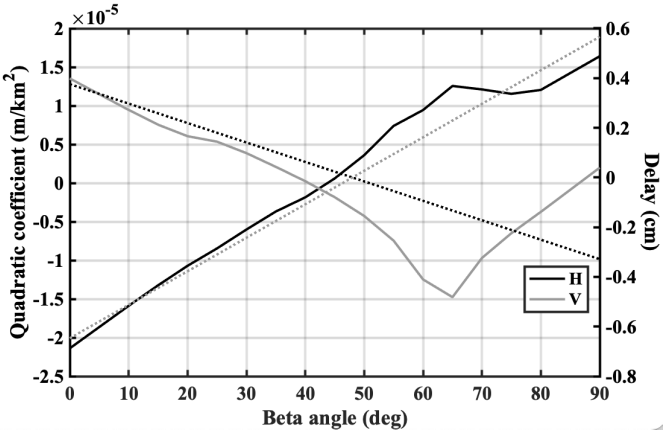

Fig. 37. Quadratic coefficient (solid) and delay (dotted) for H (black) and V (gray) swaths as a function of beta angle.

along the axis connecting the feed and reflectarray phase centers. From the structural model (Section IV-B), we also know that the feed translation along this direction is significant over beta angle (approximately 60 μm). The discrepancy could be due to the simplifications in the modeling (e.g., the antenna model did not include the mast). This indicates that more detailed analysis might be needed to fully capture the small centimeter level variability with beta angle. Note that this error does not impact the ocean performance and, for hydrology, the error is the same order of magnitude that was accounted for pre-launch. In addition, the height residual is very repeatable over beta angle and a large fraction of this error could be removed during ground processing if desired.

VII. Conclusion

We have attempted to provide an end-to-end view of the process involved in designing the KaRIn instrument, verifying its performance through ground measurements and simulations, and finally, assessing its performance in flight. KaRIn exceeds its critical random performance requirement by one order of magnitude (in units of wavenumber spectra) at the beginning of the mission, although this margin is expected to be reduced as the HPA, antennas, and radiators age. The systematic performance has been assessed using KaRIn-only data and, within those limitations, has been shown to meet its requirements.

We have demonstrated the thermoelastic stability of the KaRIn instrument, which makes it possible to maintain the relative pointing between KaRIn's antennas, separated by 10 m, to within just a few millidegrees. We have shown that our simulations were able to accurately predict the differential phase and roll drifts in the function of the thermoelastic distortion over the beta angle. However, the small centimeter-level errors would require a high-fidelity analysis. We have also presented a method to assess the attitude reconstruction performance in flight, which is critical to meeting KaRIn's and SWOT's performance requirements.

The error predictions due to wave nonlinearities appear to be in line with our pre-launch estimates, although the hydrodynamic modulation coefficient used in simulations was probably conservative. Given KaRIn's excellent thermal noise performance, KaRIn's white noise floor requirement is met for SWH close to 6 m.

Finally, we have discovered an apparent cross-track surface velocity that had not been considered pre-launch but is still a negligible error source.

No attempt has been made in this article at validating the SWOT mission error requirement. However, given KaRIn's reported performance, and the fact that KaRIn is a novel instrument in SWOT and that all other instruments have a very high level of maturity, we believe that SWOT is on the right path to meet its mission's science objectives.

Appendix
Calculation of Effective Antenna Panel Translation and Rotation

To calculate the effective antenna panel translation and rotation for each of the two antennas, we solve for the best-fit rigid-body translation and rotation that transforms the nominal antenna panel node locations into distorted node locations. Let $x_i^{(\mathrm{nom})}$ be the nominal position vector of node i and t_i the time-dependent nodal translation vector. The distorted positions $x_i^{(\mathrm{dist})}$ of each node at each time step are given by

$$x_i^{(\mathrm{dist})} = x_i^{(\mathrm{nom})} + t_i \quad \forall i. \tag{16}$$

Next, we want to solve for the best-fit rigid-body translation vector T and rotation matrix R, which would transform the nominal node locations into the distorted node locations, such that

$$x_i^{(\mathrm{dist})} \approx R x_i^{(\mathrm{nom})} + T. \tag{17}$$

To find the best-fit translation and rotation in the least-squared sense, we need to solve the mathematical optimization problem

$$\min_{T,R} \sum_{i=1}^{N} \|r_i\|^2 = \min_{T,R} \sum_{i=1}^{N} \left\| x_i^{(\mathrm{dist})} - \left(\mathrm{Rx}_i^{(\mathrm{nom})} + T \right) \right\|^2 \tag{18}$$

where the operator $\|\cdot\|$ is the usual vector 2-norm and N is the number of nodes.

This mathematical optimization problem belongs to a class of problems known as the *Procrustes problem*. We have implemented the solution to (18) given by Arun et al. [45], who point out that T is equal to the vector from the geometric centroid of the set of all $x_i^{(\mathrm{nom})}$ to the geometric centroid of the set of all $x_i^{(\mathrm{dist})}$.

Acknowledgment

The authors would like to thank Nathalie Steunou and Bertrand Raffier for significant contributions to the attitude reconstruction modeling, Gerald Dibarboure for many technical discussions on the crossover algorithm, Alejandro Bohe for his insights when carefully assessing volumetric decorrelation using Surface Water and Ocean Topography (SWOT) data, Simone Tanelli for providing APR2 data, Jinbo Wang for discussions on ocean science, and Dudley Chelton for reviewing this manuscript. They acknowledge the entire Ka-band Radar Interferometer (KaRIn) and SWOT teams that developed the flight hardware and support systems that made these measurements possible, including not only the JPL team but also our TAS, CNES, CPI, and CSA colleagues. Finally, they also thank the SWOT mission operations team for their efforts in operating SWOT and KaRIn smoothly and delivering all the fascinating data.

References

[1] R. Morrow et al., "Ocean circulation from space," *Surveys Geophys.*, vol. 44, no. 5, pp. 1243–1286, 2023.

[2] J.-F. Cretaux, K. Nielsen, F. Frappart, F. Papa, S. Calmant, and J. Benveniste, "Hydrological applications of satellite altimetryrivers, lakes, man-made reservoirs, inundated areas," in *Satellite Altimetry Over Oceans and Land Surfaces*. Boca Raton, FL, USA: CRC Press, 2017, pp. 459–504.

[3] P. Escudier et al., "Satellite radar altimetry: Principle, accuracy, and precision," in *Satellite Altimetry Over Oceans and Land Surfaces*. Boca Raton, FL, USA: CRC Press, 2017, pp. 1–70.

[4] L.-L. Fu et al., "SWOT: The surface water and ocean topography mission. Wide-swath altimetric elevation on Earth," Tech. Rep. JPL-Publ-12-5, 2012.

[5] D. E. Alsdorf, E. Rodríguez, and D. P. Lettenmaier, "Measuring surface water from space," *Rev. Geophys.*, vol. 45, no. 2, 2007. [Online]. Available: https://agupubs.onlinelibrary.wiley.com/doi/abs/10.1029/2006RG000197

[6] E. Rodriguez, D. E. Fernandez, E. Peral, C. W. Chen, J.-W. De Bleser, and B. Williams, "Wide-swath altimetry: A review," in *Satellite Altimetry Over Oceans and Land Surfaces*. Boca Raton, FL, USA: CRC Press, 2017, pp. 71–112.

[7] E. Rodriguez and J. M. Martin, "Theory and design of interferometric synthetic aperture radars," *IEE Proc. F Radar Signal Process.*, vol. 139, no. 2, p. 147, 1992.

[8] P. A. Rosen et al., "Synthetic aperture radar interferometry," *Proc. IEEE*, vol. 88, no. 3, pp. 333–382, Mar. 2000.

[9] E. Rodríguez, C. S. Morris, and J. E. Belz, "A global assessment of the SRTM performance," *Photogrammetric Eng. Remote Sens.*, vol. 72, no. 3, pp. 249–260, Mar. 2006.

[10] S. S. Board, *Earth Science and Applications From Space: National Imperatives for the Next Decade and Beyond*. Washington, DC, USA: National Academies Press, 2007.

[11] M. Durand, L.-L. Fu, D. P. Lettenmaier, D. E. Alsdorf, E. Rodriguez, and D. Esteban-Fernandez, "The surface water and ocean topography mission: Observing terrestrial surface water and oceanic submesoscale eddies," *Proc. IEEE*, vol. 98, no. 5, pp. 766–779, May 2010.
[12] S. Desai. (2018). *Swot Mission Science Requirements Document*. [Online]. Available: https://swot.jpl.nasa.gov/system/documents/files/2176_2176_D-61923_SRD_Rev_B_20181113.pdf
[13] S. Abdalla et al., "Altimetry for the future: Building on 25 years of progress," *Adv. Space Res.*, vol. 68, no. 2, pp. 319–363, 2021.
[14] C. Dufau, M. Orsztynowicz, G. Dibarboure, R. Morrow, and P. Le Traon, "Mesoscale resolution capability of altimetry: Present and future," *J. Geophys. Res., Oceans*, vol. 121, no. 7, pp. 4910–4927, Jul. 2016.
[15] D. Esteban-Fernandez. (2017). *SWOT Mission Performance & Error Budget*. [Online]. Available: https://swot.jpl.nasa.gov
[16] G. Dibarboure et al., "Data-driven calibration algorithm and pre-launch performance simulations for the SWOT mission," *Remote Sens.*, vol. 14, no. 23, p. 6070, Nov. 2022.
[17] T. G. Farr et al., "The shuttle radar topography mission," *Rev. Geophys.*, vol. 45, no. 2, 2007. [Online]. Available: https://agupubs.onlinelibrary.wiley.com/doi/abs/10.1029/2005RG000183
[18] J. C. Curlander and R. N. McDonough, *Synthetic Aperture Radar*, vol. 11. New York, NY, USA: Wiley, 1991.
[19] J. J. Kovaly, *Synthetic Aperture Radar*. Dedham, MA, USA: Artech House, 1976.
[20] R. E. Hodges, J. C. Chen, M. R. Radway, L. R. Amaro, B. Khayatian, and J. Munger, "An extremely large Ka-band reflectarray antenna for interferometric synthetic aperture radar: Enabling next-generation satellite remote sensing," *IEEE Antennas Propag. Mag.*, vol. 62, no. 6, pp. 23–33, Dec. 2020.
[21] W. Harvey, M. Tope, D. Esteban-Fernandez, A. Roitman, E. Sokol, and D. Berry, "Development path of a Ka-band extended interaction klystron for space-borne interferometer," in *Proc. IEEE Int. Vac. Electron. Conf. (IVEC)*, Apr. 2016, pp. 1–2.
[22] J. Huang, "Microstrip reflectarray," in *Proc. Antennas Propag. Soc. Symp. Dig.*, 1991, pp. 612–615.
[23] D. Vandemark, B. Chapron, J. Sun, G. H. Crescenti, and H. C. Graber, "Ocean wave slope observations using radar backscatter and laser altimeters," *J. Phys. Oceanogr.*, vol. 34, no. 12, pp. 2825–2842, Dec. 2004.
[24] E. Peral. (2021). *Karin: Ka-Band Radar Interferometer On-Board Processor Algorithm Theoretical Basis Document*. [Online]. Available: https://swot.jpl.nasa.gov
[25] G. Franceschetti and R. Lanari, *Synthetic Aperture Radar Processing*. Boca Raton, FL, USA: CRC Press, 1999.
[26] R. Ahmed, D. Esteban-Fernández, and S. Hensley, "Analytical models for multipath and switch leakage for the SWOT interferometer," *Sensors*, vol. 22, no. 5, p. 1931, Mar. 2022.
[27] A. Bohé, "A complete theoretical derivation of the level of random height noise in interferometric unfocused SAR swath altimetry," *IEEE Trans. Geosci. Remote Sens.*, vol. 61, pp. 1–29, 2023, Art. no. 5215229, doi: 10.1109/TGRS.2023.3290850.
[28] C. W. Chen, "A spectral model for multilook InSAR phase noise due to geometric decorrelation," *IEEE Trans. Geosci. Remote Sens.*, vol. 61, pp. 1–11, 2023, Art. no. 5207611, doi: 10.1109/TGRS.2023.3272296.
[29] E. Peral, E. Rodríguez, and D. Esteban-Fernández, "Impact of surface waves on SWOT's projected ocean accuracy," *Remote Sens.*, vol. 7, no. 11, pp. 14509–14529, Nov. 2015.
[30] S. Sabah and R. Lorenz, "Design and calibration of IQ-mixers," in *Proc. EPAC*, vol. 98, 1998, p. 1589.
[31] D. W. Nicholson, *Finite Element Analysis: Thermomechanics of Solids*. Boca Raton, FL, USA: CRC Press, 2008.
[32] A. Khennane, *Introduction to Finite Element Analysis Using MATLAB® and Abaqus*. Boca Raton, FL, USA: CRC Press, 2013.
[33] Ansys. *Ansys Hfss 3D High Frequency Structure Simulation Software*. Accessed: Dec. 2023. [Online]. Available: https://www.ansys.com/products/electronics/ansys-hfss
[34] D. M. Pozar and T. A. Metzler, "Analysis of a reflectarray antenna using microstrip patches of variable size," *Electron. Lett.*, vol. 29, no. 8, p. 657, 1993.
[35] D. M. Pozar, S. D. Targonski, and H. D. Syrigos, "Design of millimeter wave microstrip reflectarrays," *IEEE Trans. Antennas Propag.*, vol. 45, no. 2, pp. 287–296, Feb. 1997.
[36] S. R. Rengarajan, "Choice of basis functions for accurate characterization of infinite array of microstrip reflectarray elements," *IEEE Antennas Wireless Propag. Lett.*, vol. 4, pp. 47–50, 2005.
[37] S. Tanelli. *Airborne Precipitation Radar 2nd Generation*. Accessed: Dec. 2023. [Online]. Available: https://airbornescience.jpl.nasa.gov/instruments/apr2apr3
[38] F. Wong and I. G. Cumming, "A combined SAR Doppler centroid estimation scheme based upon signal phase," *IEEE Trans. Geosci. Remote Sens.*, vol. 34, no. 3, pp. 696–707, May 1996.
[39] G. Huffman, D. Bolvin, D. Braithwaite, K. Hsu, R. Joyce, and P. Xie. (2014). *2014: Integrated Multi-Satellite Retrievals for GPM (Imerg), Version 4.4. NASA's Precipitation Processing Center, Accessed 31, Mar. 2015*. Accessed: Mar. 31, 2015. [Online]. Available: http://arthurhou.pps.eosdis.nasa.gov/gpmdata/
[40] R. Owens and T. Hewson. *ECMWF Forecast User Guide*. Accessed: Dec. 2023. [Online]. Available: https://www.ecmwf.int/en/elibrary/81307-ecmwf-forecast-user-guide
[41] SWOT. (2023). *Swot Level 2 Karin Low Rate Sea Surface Height Data Product Version 1.1*. [Online]. Available: https://podaac.jpl.nasa.gov/dataset/SWOT_L2_LR_SSH_1.1
[42] B. Chapron, F. Collard, and F. Ardhuin, "Direct measurements of ocean surface velocity from space: Interpretation and validation," *J. Geophys. Res., Oceans*, vol. 110, no. C7, 2005. [Online]. Available: https://agupubs.onlinelibrary.wiley.com/doi/pdf/10.1029/2004JC002809
[43] I. Fenty and O. Wang. (2020). *Ecco Ocean Velocity—Daily Mean Llc90 Grid (Version 4 Release 4)*. [Online]. Available: https://podaac.jpl.nasa.gov/dataset/ECCO_L4_OCEAN_VEL_LLC0090GRID_DAILY_V4R4
[44] ECMSI (CMEMS). (2023). *Global Ocean Gridded L4 Sea Surface Heights*. [Online]. Available: https://data.marine.copernicus.eu/product/SEALEVEL_GLO_PHY_L4_NRT_008_046/description
[45] K. S. Arun, T. S. Huang, and S. D. Blostein, "Least-squares fitting of two 3-D point sets," *IEEE Trans. Pattern Anal. Mach. Intell.*, vol. PAMI-9, no. 5, pp. 698–700, Sep. 1987.

Eva Peral received the B.S. and Ph.D. degrees in telecommunications engineering from the Universidad Politécnica de Valencia, Valencia, Spain, in 1995 and 1998, respectively, and the M.S. and Ph.D. degrees in electrical engineering from California Institute of Technology, Pasadena, CA, USA, in 1998 and 2000, respectively.

Since 2009, she has been with the NASA Jet Propulsion Laboratory, California Institute of Technology, where she was the Technical Group Supervisor with the Digital Radar Electronics Group from 2012 to 2017 and is currently a Principal Staff Engineer. She led the RainCube mission, the first-ever radar in a CubeSat, as the Principal Investigator and an Instrument Manager. Since 2017, she has been the Lead Instrument System Engineer for the Ka-band Radar Interferometer of the SWOT mission. She holds nine U.S. patents and has authored over 40 peer-reviewed publications and one book chapter. She has over 25 years of research experience in the areas of radar system engineering, radar onboard processing, optoelectronics, and fiber optical communications.

Daniel Esteban-Fernández received the Ph.D. degree in electrical engineering from the University of Massachusetts at Amherst, Amherst, MA, USA, in 2005.

He is currently the Manager of the Communications, Tracking and Radar Division, Jet Propulsion Laboratory (JPL), California Institute of Technology, Pasadena, CA, USA. He has been the Instrument Manager for the Ka-band Radar Interferometer (KaRIn) since 2017. Previously, he was a Lead Systems Engineer on the Surface Water and Ocean Topography (SWOT) mission for KaRIn. Over his career at JPL, he also served as a Payload System Engineer for Jason-3 and a Cognizant Engineer for its laser retroreflector array (LRA) instrument and has participated in many radar mission concept studies and technology development tasks. Before coming to JPL, he worked at the National Oceanic and Atmospheric Administration, Silver Spring, MD, USA, on remote microwave sensing of hurricanes.

Ernesto Rodríguez, photograph and biography not available at the time of publication.

Dalia McWatters is currently a JPL radar Instrument Engineer with JPL, California Institute of Technology, Pasadena, CA, USA, with 39 years of experience, having worked on the full life cycle of successful space radar mapping missions: Shuttle Radar Topography Mission (SRTM), Aquarius, and Surface Water and Ocean Topography (SWOT). She is working on the INvestigation of Convective UpdraftS (INCUS) NASA Earth Ventures Mission.

Jan-Willem De Bleser received the M.S.E. and Ph.D. degrees from KU Leuven, Leuven, Belgium, in 2007 and 2013, respectively, both in electrical engineering specializing in telecommunications and telematics.

Since 2014, he has been with the Radar Section, Jet Propulsion Laboratory, California Institute of Technology, Pasadena, CA, USA, as an Instrument System Engineer. He has worked continually on Surface Water and Ocean Topography (SWOT) in both system engineering and algorithms since the preliminary design phase, as a Deputy Instrument System Engineer during commissioning. More generally, he has been involved in the development of systems and algorithms for InSAR, tomography, and scatterometry.

Razi Ahmed received the B.S.E.E. degree from the National University of Sciences and Technology, Islamabad, Pakistan, in 2002, and the M.S. and Ph.D. degrees in electrical and computer engineering from the University of Massachusetts at Amherst, Amherst, MA, USA, in 2012.

He has been a Technical Supervisor with the Radar System and Instrument Engineering Group, Jet Propulsion Laboratory, California Institute of Technology, Pasadena, CA, USA, since 2022. His research interests include spaceborne radar remote sensing, synthetic aperture radar (SAR) interferometry and polarimetry, tomography, altimetry, and weather radars.

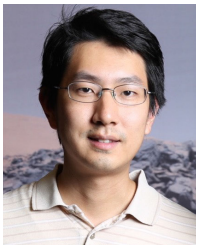

Albert C. Chen received the B.S.E. degree from the University of Michigan, Ann Arbor, MI, USA, in 2006, and the M.S. and Ph.D. degrees from Stanford University, Stanford, CA, USA, in 2008 and 2013, respectively, all in electrical engineering.

As a Post-Doctoral Scholar at the Department of Geophysics, Stanford University, he studied permafrost in Alaska using both repeat-pass InSAR and ground-penetrating radar. He is currently a Signal Analysis Engineer with the Radar System and Instrument Engineering Section, NASA Jet Propulsion Laboratory (JPL), California Institute of Technology, Pasadena, CA, USA, in 2015. His research interests include interferometric synthetic aperture radar remote sensing, signal processing, and scientific computation.

Eric Slimko, photograph and biography not available at the time of publication.

Ruwan Somawardhana has extensive thermal systems flight hardware and design experience, including concept studies, design and analysis, fabrication, integration, testing, and flight operations. He was the SWOT Payload Thermal Systems Lead Engineer for 11 years supporting the preliminary design through a successful launch and on-orbit commissioning.

Kevin Knarr, photograph and biography not available at the time of publication.

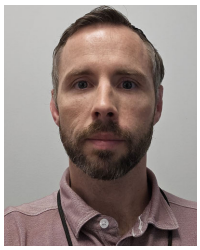

Michael Johnson received the B.S. degree in electrical engineering from California State Polytechnic University, Pomona, CA, USA, in 2006, and the M.S. degree in electrical engineering from Stanford University, Stanford, CA, USA, in 2012.

As a Signal Analysis Engineer at the NASA Jet Propulsion Laboratory, California Institute of Technology, Pasadena, CA, USA, his areas of work have included developing remote sensing simulation systems and data analysis software for flight hardware testing. His research interests include data science and applications of machine learning for remote sensing.

Sermsak Jaruwatanadilok received the B.E. degree in telecommunication engineering from the King Mongkut's Institute of Technology, Lad Krabang, Thailand, in 1994, the M.S. degree in electrical engineering from Texas A&M University, College Station, TX, USA, in 1997, and the Ph.D. degree in electrical engineering from the University of Washington, Seattle, WA, USA, in 2003.

From 2006 to 2010, he was a Research Assistant Professor at the University of Washington. He is currently a Signal Analysis Engineer at the Jet Propulsion Laboratory, California Institute of Technology, Pasadena, CA, USA. His research interests include electromagnetic wave propagation in random and complex media and remote sensing.

Samuel Chan, photograph and biography not available at the time of publication.

Xiaoqing Wu received the B.S. and M.S. degrees in electrical engineering from Nanjing University of Aeronautics and Astronautics, Nanjing, China, in 1982 and 1985, respectively, and the Ph.D. degree in electrical engineering from the University of Stuttgart, Stuttgart, Germany, in 1998.

He was involved in data system design and development for the Modified Antarctic Mapping Mission and contributed to producing the first Antarctic surface velocity map and the interferometric coherence map while he worked from 1998 to 2008 at Vexcel Corporation, Boulder, CO, USA. He joined the Jet Propulsion Laboratory, California Institute of Technology, Pasadena, CA, USA, in 2008, and has produced the first radar image of Greenland ice sheet bed. He has been involved in NASA's Surface Water and Ocean Topography (SWOT) mission, IceBridge mission, AirSWOT, Glistin, and GISMO projects with extensive experience in synthetic aperture radar (SAR) data processing and analysis.

Duane Clark, photograph and biography not available at the time of publication.

Kenneth Peters received the B.S.E.E. degree from the University of Rochester, Rochester, NY, USA, in 1987, and the M.S.E.E. degree from California Institute of Technology, Pasadena, CA, USA, in 1989.

He is currently the Flight Software Lead for the Surface Water and Ocean Topography (SWOT) Ka-band Radar Interferometer (KaRIn). Other work includes software design and development for the Space Telecommunications Radio System (STRS), Electra radios on several past and upcoming Mars orbiters and landers, Shuttle Radar Topography Mission (SRTM), and Search for Extraterrestrial Intelligence (SETI). He is also a member of the JPL Software Engineering Management Oversight Group (SEMOG), California Institute of Technology.

Curtis W. Chen received the dual B.S. and A.B. degree in electrical engineering and political science and the M.S. and Ph.D. degrees in electrical engineering from Stanford University, Stanford, CA, USA, in 1996, 1999, and 2001, respectively.

He developed new algorithms for 2-D phase unwrapping of interferometric synthetic aperture radar (SAR) data at Stanford University. Since 2001, he has been with the NASA Jet Propulsion Laboratory, California Institute of Technology, Pasadena, CA, USA, where he has been involved in radar sensors for Mars landers and SAR/InSAR instruments for Earth-science missions.

Peter Mao, photograph and biography not available at the time of publication.

Behrouz Khayatian received the B.S. degree from Brigham Young University, Provo, UT, USA, in 1989, the M.S. degree from The Ohio State University, Columbus, OH, USA, in 1992, and the Ph.D. degree from the University of California at Los Angeles, Los Angeles, CA, USA, in 2003, all in electrical engineering.

From 1996 to 2001, he worked as a Senior RF System Engineer at AT&T, Tustin, CA, USA. Since 2001, he has been a Senior Microwave and Antenna Engineer with the Communications Ground Section, Jet Propulsion Laboratory, California Institute of Technology, Pasadena, CA, USA. He has also served as a CogE, System, and Antenna/Microwave Engineer for various spacecraft and mission proposals, including Surface Water and Ocean Topography (SWOT), JUNO, Aquarius, Jason-3 and Jason-2, Mars Science Laboratory (MSL), NISAR, SAFIR, and a number of ground communication applications involving NASA's Deep Space Network (DSN) for 34- and 70-m Beam WaveGuide (BWG) antennas. His research interests include microwave and antenna component design, electromagnetic scattering, and high-power RF systems.

Jacqueline Chen is currently a Senior Project Engineer with the Jet Propulsion Laboratory, California Institute of Technology, Pasadena, CA, USA, responsible for the development of key flight antennas, such as the Surface Water and Ocean Topography (SWOT) reflectarray and JUNO radiometer antennas. Currently, she is working on Venus missions for VERITAS VISAR interferometer antenna and Envision VenSAR radar antenna.

Richard E. Hodges (Life Senior Member, IEEE) received the B.S.E.E. degree from The University of Texas at Austin, Austin, TX, USA, in 1978, the M.S.E.E. degree from California State University at Northridge, Northridge, CA, USA, in 1987, and the Ph.D.E.E. from the University of California at Los Angeles, Los Angeles, CA, USA, in 1996.

His career has included work at Hughes Aircraft Company, Culver City, CA, USA; Rantec Microwave Systems, Westlake Village, CA, USA; Raytheon, McKinney, TX, USA; and the Jet Propulsion Laboratory (JPL), California Institute of Technology, Pasadena, CA, USA. He served as the Technical Group Supervisor of JPL's Spacecraft Antennas Group from 2002 to 2018 and is currently a Principal Staff Engineer. He led Raytheon's DARPA RECAP program, which developed the world's first decade bandwidth (10:1) electronic scanned array antenna. At JPL, he created the original design architecture for the JUNO mission radiometer antennas, was the Principal Investigator for the ISARA mission, designed the first two reflectarray antennas flown in space (for the ISARA and MarCO missions), created the SweepSAR scanning reflector design concept for the NISAR mission, and was the Co-Investigator responsible for the RainCube deployable mesh reflector antenna. He developed the original reflectarray antenna design for the Surface Water and Ocean Topography (SWOT) mission and created antenna designs for both the VERITAS and EnVision Venus radar mapping missions. He has published over 100 refereed journal articles and conference papers, three book chapters, and holds seven U.S. patents.

Dr. Hodges received the IEEE Antenna and Propagation Society's Schelkunoff Best Paper Award in 2017.

Dhemetrios Boussalis, photograph and biography not available at the time of publication.

Bryan Stiles, (Member, IEEE), photograph and biography not available at the time of publication.

Karthik Srinivasan, photograph and biography not available at the time of publication.